

# Stress-relaxing granular bioprinting materials enable complex and uniform organoid self-organization

Received: 9 October 2024

Accepted: 26 January 2026

Published online: 10 March 2026

 Check for updates

Austin J. Graham <sup>1,2</sup>, Michelle W. L. Khoo <sup>2</sup>, Vasudha Srivastava <sup>1</sup>, Sara Viragova <sup>3</sup>, Honesty Kim<sup>1,2</sup>, Kavita Parekh <sup>4</sup>, Kelsey M. Hennick <sup>5</sup>, Malia Bird <sup>1</sup>, Nadine Goldhammer <sup>6</sup>, Jie Zeng Yu <sup>6</sup>, Grace Hu <sup>7</sup>, Natasha T. Brinkley <sup>7</sup>, Lucas Pardo<sup>7</sup>, Jasmine S. Amaya <sup>4</sup>, Cameron D. Morley<sup>4</sup>, Nishant Chadha<sup>5</sup>, Paul Lebel <sup>2</sup>, Sanjay Kumar <sup>4,8,9</sup>, Jennifer M. Rosenbluth<sup>2,6</sup>, Tomasz J. Nowakowski<sup>5</sup>, Ovijit Chaudhuri <sup>10,11</sup>, Ophir Klein<sup>3,12</sup>, Rafael Gómez-Sjöberg <sup>2</sup>  & Zev J. Gartner <sup>1,2,9,13</sup> 

Complex and robust tissue self-organization requires defined initial conditions and dynamic boundaries—neighbouring tissues and extracellular matrix that actively evolve to guide morphogenesis. A major challenge in tissue engineering is identifying material properties that are compatible with controlling initial culture conditions while mimicking dynamic tissue boundaries. Here we describe a highly tunable granular biomaterial, MAGIC matrix, that supports both long-term bioprinting and gold-standard tissue self-organization. We identify that significant stress relaxation at the long timescales and large deformation magnitudes relevant to self-organization is required for optimal morphogenesis. We apply optimized MAGIC matrices toward precise extrusion bioprinting of saturated cell suspensions directly into three-dimensional culture. Carefully controlling initial conditions for tissue growth yields dramatic increases in organoid reproducibility and complexity across multiple tissue types, enabling high-throughput generation of organoid arrays and perfusable three-dimensional micro-physiological systems. Our results identify key biomaterial parameters for optimal organoid morphogenesis and lay the foundation for fabricating more complex and reproducible self-organized tissues.

Controlling the uniformity and complexity of tissues grown in vitro remains a major challenge<sup>1,2</sup>. Tissues in vivo typically self-organize juxtaposed to other tissues that act as living boundaries, changing shape and composition in parallel to direct morphogenesis<sup>3</sup>. Guiding tissue self-organization in vitro requires replicating the important functional characteristics of these living interfaces, and satisfying these requirements remains a major challenge in materials science and tissue engineering<sup>4</sup>. Non-living biomaterials attempt to replicate key chemical and rheological

cues derived from living boundaries, with gold standards including reconstituted basement membrane matrices (rBMs) such as Matrigel<sup>5</sup>. For rBMs, recent studies have highlighted the presence of laminin epitopes and soft viscoelastic rheological properties as essential for epithelial polarity and morphogenesis<sup>6,7</sup>. This has enabled the design of synthetic biomaterials that support symmetry breaking during self-organization<sup>1,8–13</sup>. However, the quantitative relationships between biomechanical properties and outcomes of morphogenesis remain unclear.

A full list of affiliations appears at the end of the paper.  e-mail: [rafael.gomez@czbiohub.org](mailto:rafael.gomez@czbiohub.org); [zev.gartner@ucsf.edu](mailto:zev.gartner@ucsf.edu)

An additional challenge to directing the uniform and complex self-organization of tissues *in vitro* is setting the initial conditions of a culture—defined here as the total number of cells, the proportions of each cell type and their positions in three-dimensional (3D) space. *In vivo*, each stage in morphogenesis emerges from a limited set of initial conditions, and large changes in initial conditions can have a profound impact on growth outcomes<sup>2</sup>. To control initial conditions engineers have developed platforms such as microwell arrays, microphysiological systems and 3D bioprinting that can be deployed together with biomaterials to further constrain self-organization<sup>14–16</sup>. Typically, however, these engineered systems are incompatible with the optimal rheological properties for tissue morphogenesis, requiring that tissues are transferred between different materials after fabrication (for example, microwells) or that their structure remains static within the device (for example, microphysiological systems).

Among engineering platforms, embedded 3D bioprinting of saturated cell suspensions provides remarkable flexibility for ‘writing’ the initial conditions of tissue morphogenesis<sup>17–20</sup>. However, much of biomaterial design for 3D printing has focused on optimizing complex geometries while sustaining cell viability and simple behaviours such as growth and motility. When the goal is to build tissues, however, active mechanical processes such as lumenization, inflation, compaction, cell sorting and folding that contribute to the final tissue form are equally important<sup>17,21,22</sup> (Fig. 1a). Although rBMs support these behaviours, and Matrigel has been used as an embedded bioprinting material<sup>17</sup>, they have several critical limitations preventing generation of tissues of high complexity or in high throughput.

As an alternative, granular microgels are frequently applied as embedded 3D bioprinting materials because they can support the structure of extruded materials after printing<sup>23,24</sup>. A critical feature of these materials is reversible yield-stress behaviour, in which the granular microgels yield in response to the printhead and extruded material, then recover to provide elastic support to the bioink. However, most granular materials are not optimal for long-term cell health, and little is known about whether the properties necessary for bioprinting are compatible with complex tissue morphogenesis<sup>25</sup>. Several groups have introduced interstitial matrices derived from natural extracellular matrix (ECM) such as collagen I to improve cell survival and dynamics<sup>26–28</sup>. However, the rheological properties and chemical composition of the resulting materials can limit self-organization. For example, collagen I-containing ECM is not optimized to support epithelial growth and morphogenesis compared to rBMs<sup>17</sup>.

In this study, we quantify the relationship between granular biomaterial rheology and tissue self-organization to reveal that when controlling for modulus at short timescales, the rate and extent of stress relaxation at long timescales determines the quantitative outcome of tissue morphogenesis. We apply this insight to design an optimized embedded bioprinting material termed Matrigel-Alginate Granular-Interstitial Composite (MAGIC) matrix. MAGIC matrices

employ alginate microgels that are optically transparent and approximately cell-sized, facilitating yielding behaviour, high-fidelity embedded bioprinting, imaging and organoid growth. Utilizing Matrigel as the interstitium creates a composite matrix that fluidizes upon shear at 4 °C to allow for long print times ( $\geq 2$  h), but cross-links at 37 °C to create an environment with similar rheology to pure Matrigel across several metrics. We find that MAGIC matrices are remarkably tunable across properties including yield-stress, shear modulus and stress relaxation at short and long timescales. To capitalize on the reproducibility, scalability and automation afforded by 3D printing into MAGIC matrices, we designed a piezoelectric bioprinting platform that allows for full *xyz* control, real-time imaging and flexible print geometries to control the initial conditions of organoid self-organization. Together, MAGIC matrix bioprinting led to nearly 100% organoid formation efficiency, dramatic improvements in interorganoid homogeneity, orders-of-magnitude improvement in the statistical power of phenotypic assays, and enabled patterning of perfusable 3D microphysiological systems.

## Results

### MAGIC matrices can be tuned for optimal 3D patterning at 4 °C

Matrigel is the gold-standard biomaterial for supporting the complex morphogenesis of epithelial organoids. However, it does not support long bioprinting windows (Supplementary Movie 1). When extruding a cell-dense bioink as it warms from 4 °C to room temperature (as previously described<sup>17</sup>), Matrigel is initially too liquid to support printed cells and filaments settle to the bottom of the dish after extrusion (Fig. 1b.1). During a narrow span of  $\sim 2$  min during gelation, the bath supports printed shapes (Fig. 1b.2), after which the gel became too elastic and cells are not extruded or ejected from the printing plane (Fig. 1b.3). We therefore sought to design a reversible yield-stress granular material that supported embedded bioprinting at 4 °C but could be tuned to match the rheological properties of biomaterials such as Matrigel at 37 °C. For the granular phase we turned to alginate as an optically transparent biomaterial that is largely inert in mammalian culture and has been used in both bioprinting and organoid culture applications<sup>26,29</sup>. We used microgels that were approximately cell sized to facilitate self-organization, migration and diffusion<sup>27</sup> (Extended Data Fig. 1). We supplemented the microgels with an interstitial matrix of Matrigel because its rich chemical composition is necessary to support morphogenesis of most epithelial organoids. At 4 °C, this material supported bioprinting of cell-dense bioinks for  $>2$  h without compromising print fidelity (Fig. 1c). We termed this class of composite materials MAGIC matrix (Fig. 1d,e).

The composite biomaterial was tunable along several rheological parameters and in different temperature regimes to support bioprinting and tissue morphogenesis. To demonstrate this tunability we prepared several compositions and characterized their

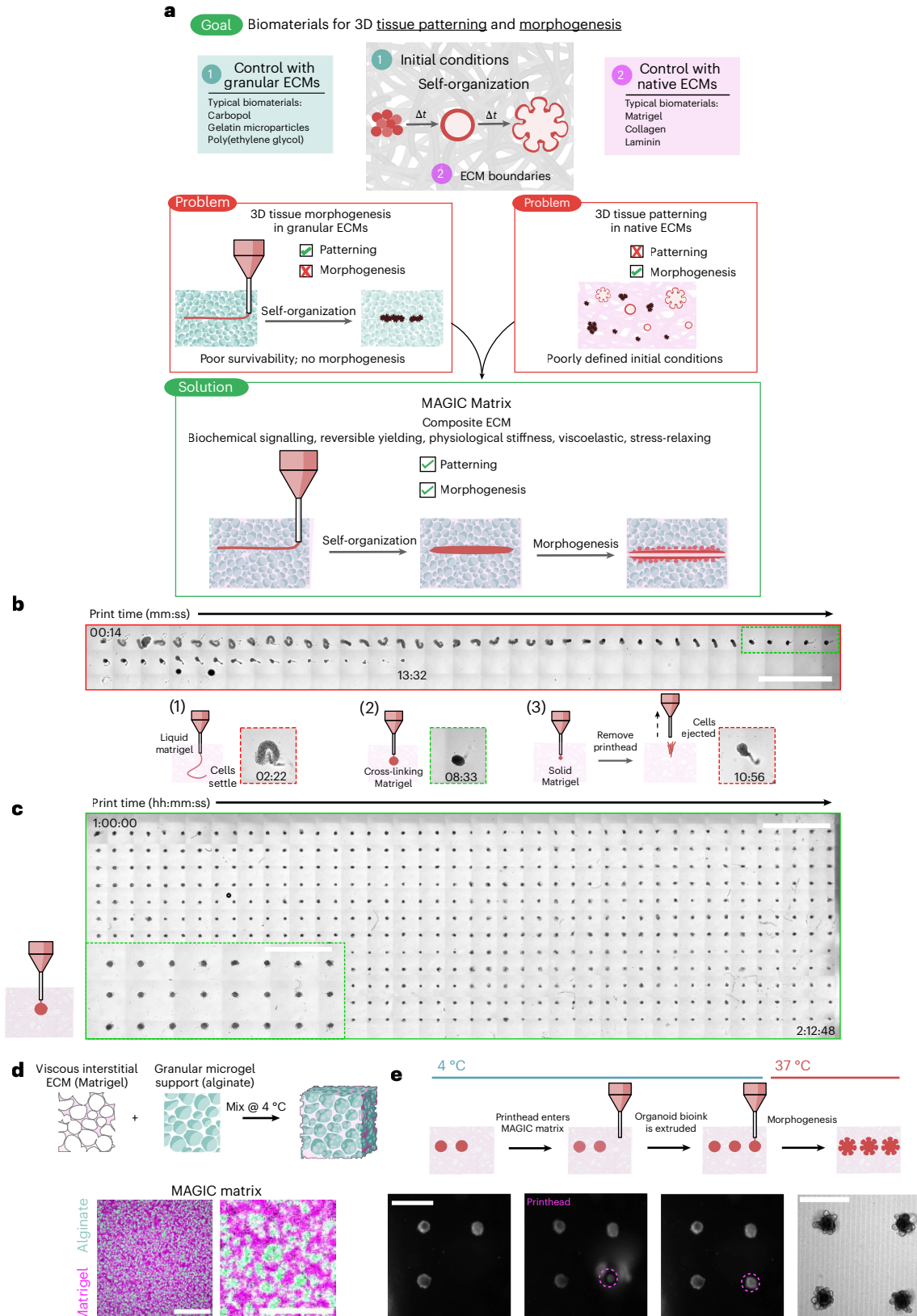
### Fig. 1 | MAGIC extracellular matrices are embedded bioprinting materials that enable both patterning and morphogenesis of organoids. a, Biomaterials designed for tissue patterning, such as some hydrogel microparticles, fail to support long-term tissue health or complex behaviours such as morphogenesis. Biomaterials typically used for such behaviours include Matrigel and collagen, but these materials do not mechanically support embedded bioprinting. MAGIC matrices exhibit a suite of biochemical and mechanical behaviours that, in sum, enable both complex patterning and morphogenesis of organoid bioinks.

**b**, Organoid slurries printed into Matrigel while cross-linking at room temperature first distort and settle to the bottom of the dish (1) due to insufficient mechanical support, followed by a narrow regime ( $\sim 2$  min) during which printing is viable (2), and eventually are ejected or excluded as the hydrogel sets (3). Insets: examples of each regime. Scale bar, 4 mm. **c**, Organoid bioink printed into MAGIC matrix at 4 °C conforms to the desired morphology due its reversible yield-stress properties, enabling printing of many organoids

( $n = 528$ ) over long times ( $t > 2$  h). MAGIC matrix was left in chilled conditions on the printer for 1 h before printing to demonstrate printing longevity. Scale bar, 4 mm. Inset: zoomed view of organoids printed in MAGIC matrix. Scale bar, 2 mm. **d**, MAGIC matrix comprises of an inert alginate microgel granular support and a viscous basement membrane interstitium. Confocal microscopy images showing a standard MAGIC matrix composition using FITC-alginate microgels and NHS-labelled Matrigel. Scale bar, 100  $\mu\text{m}$ . Zoomed view shows white pixels where fluorescent signals overlap, suggesting ECM in alginate microgels. Scale bar, 40  $\mu\text{m}$ . **e**, Sequential bright-field images demonstrating MAGIC matrix bioprinting, in which the printhead enters cold MAGIC matrix, extrudes organoid slurry and is then removed from the matrix, leaving a geometrically and spatially controlled feature behind. These organoid bioinks subsequently undergo self-organization at 37 °C to form mature organoids. Scale bars, 500  $\mu\text{m}$ . Diagram in **d** created in BioRender; Graham, A. <https://BioRender.com/chloelz> (2026).

properties by shear rheology at 4 °C (relevant to bioprinting) and 37 °C (relevant to organoid culture). Preparations included undiluted jammed alginate microgels (AMGs); three different volume fractions of AMG slurry diluted in Matrigel at 2:1, 1:1 and 1:2 AMGs:Matrigel by added volume; and two different polymer weight fractions in the AMG preparation at 0.5 and 1 wt%. All compositions of MAGIC matrix demonstrated reversible yield-stress behaviour at 4 °C and fitted well

to a Herschel–Bulkley exponential model, suggesting their utility as embedded bioprinting materials (Fig. 2a). Varying MAGIC matrix composition tuned yield-stress values over an order of magnitude (Fig. 2b). Viscoelasticity and yield-stress were increased when using a viscous interstitial material such as Matrigel as opposed to cell culture media (Extended Data Fig. 2), highlighting the importance of the interstitial phase in granular materials at 4 °C (ref. 30).



## Stress relaxation over length- and time-scales relevant to morphogenesis drive crypt self-organization

To assess MAGIC matrix behaviour under physiological conditions, we next measured viscoelastic properties following cross-linking at 37 °C. At 1 wt% alginate, the storage and loss moduli of the composite matrix were significantly greater compared with pure Matrigel (Fig. 2c). In contrast, at 0.5 wt% alginate, moduli of the composite matrix were similar to that of pure Matrigel across a range of compositions (Fig. 2d). These analyses suggested that 0.5 wt% MAGIC matrices had similar rheological properties to Matrigel, and therefore, may equivalently support tissue growth and morphogenesis.

We evaluated the performance of these ECMs in morphogenesis assays using mouse duodenal organoids. Intestinal organoid crypt budding and lumen expansion is highly sensitive to matrix mechanics<sup>5,31–33</sup>. We therefore measured crypt width and length across all matrix formulations in manual dome culture (Fig. 2e). All organoids in MAGIC matrices containing 1 wt% AMGs formed shorter and wider crypts than Matrigel controls, consistent with their increased stiffness (Extended Data Fig. 3). Similarly, composite matrices formulated with both with 25% Matrigel and 1 mg ml<sup>-1</sup> collagen I were significantly stiffer than 0.5 wt% MAGIC matrices and gave rise to organoids with minimal or no crypts<sup>26</sup> (Extended Data Fig. 4). In contrast, MAGIC matrix compositions with 0.5 wt% at 50% AMG volume fraction or lower were indistinguishable from those grown in pure Matrigel (Fig. 2f).

We were surprised to find that formulations of MAGIC sharing 0.5 wt% microgels but having different volume fractions of Matrigel had different crypt morphologies despite their nearly identical storage and loss moduli. Specifically, 2:1 AMGs:Matrigel had significantly shorter and wider crypts compared with 1:1 MAGIC and Matrigel (Fig. 2g and Extended Data Fig. 3). These findings were not a consequence of Matrigel dilution, indicating that potential differences in the concentration of the interstitial ECM did not contribute to these observations (Extended Data Fig. 3). We noted that intestinal organoids undergo large morphological changes over hour timescales during morphogenesis, including crypt budding and lumen inflation<sup>33</sup>, which induce large mechanical strains in the surrounding hydrogel. Additionally, stress relaxation over these timescales affects single-cell behaviours<sup>34–36</sup> and is required for symmetry-breaking events at the tissue scale<sup>7,37–40</sup>. Thus, we hypothesized that crypt morphology may be quantitatively linked to stress-relaxation rate and magnitude at long timescales and large strains, even when the response of the materials at short length scales and timescales was identical. This hypothesis was not previously testable because previous investigations of stress relaxation used materials whose stress-relaxation rate was correlated with loss tangent<sup>34–38</sup>.

To test this hypothesis, we first measured stress relaxation of Matrigel over 1 h at variable strain. Notably, Matrigel completely relaxed accumulated stresses in ~15 min for a variety of strain magnitudes,

whereas undiluted AMGs did not (Fig. 2h). We next investigated the relevant length scale of stress relaxation for intestinal organoid morphogenesis by quantifying organoid perimeter growth over time<sup>41</sup>. Over 1-h segments we observed an average perimeter expansion of ~10% (Fig. 2i,j). Importantly, these changes in organoid size occur over timescales much longer than standard biomaterial measurement regimes (~1 Hz).

We then compared stress-relaxation properties of 1:1 and 2:1 MAGIC matrix formulations given that these compositions had matched moduli but exhibited striking differences in crypt morphology. For small deformations (approximated as 1% strain), MAGIC matrices dissipated stress nearly identically over both short and long timescales (Fig. 2k). Although both formulations dissipated stress more slowly than pure Matrigel, they ultimately dissipated 80–90% of accumulated stress after 1 h. For larger deformations relevant to organoid morphogenesis (10% strain), stress relaxation of both MAGIC formulations and Matrigel occurred nearly identically at short timescales ( $\leq 10$  s) (Fig. 2l). However, over longer times (10% strain over 1 h), 2:1 MAGIC matrices relaxed stress significantly more slowly than both Matrigel and 1:1 MAGIC, providing a potential explanation for their differential effects on organoid morphogenesis (Fig. 2m). We quantified this effect using a stretched exponential function to calculate average relaxation time for each composition<sup>36</sup> (Fig. 2m and Supplementary Information, section 2). Critically, 1:1 MAGIC matrices dissipated ~95% of internal stresses after 1 h, with as little as ~0.2 Pa of residual stress remaining in the material. This bulk property of the materials was further explored at the micrometre scale by performing nanoindentation to measure stress relaxation, where we observed impeded relaxation in 2:1 MAGIC matrix compared with 1:1 MAGIC and Matrigel (Extended Data Fig. 4). Notably at this scale, 1:1 MAGIC matrix and Matrigel relaxed stress at a similar rate and magnitude.

To establish that these properties of MAGIC matrix translated to a 3D bioprinting context, we used a bioink derived from a saturated suspension of dissociated intestinal organoids (see next section). Crypts appeared more slowly in 2:1 MAGIC matrix than in 1:1 matrix, suggesting that the rate of crypt morphogenesis may also be impacted by stress relaxation (Fig. 2n). Taken together, these results demonstrate that for materials matched in viscoelasticity at short length scales and timescales, differences in mechanical properties at long timescales and large strains can profoundly impact complex biological processes such as morphogenesis.

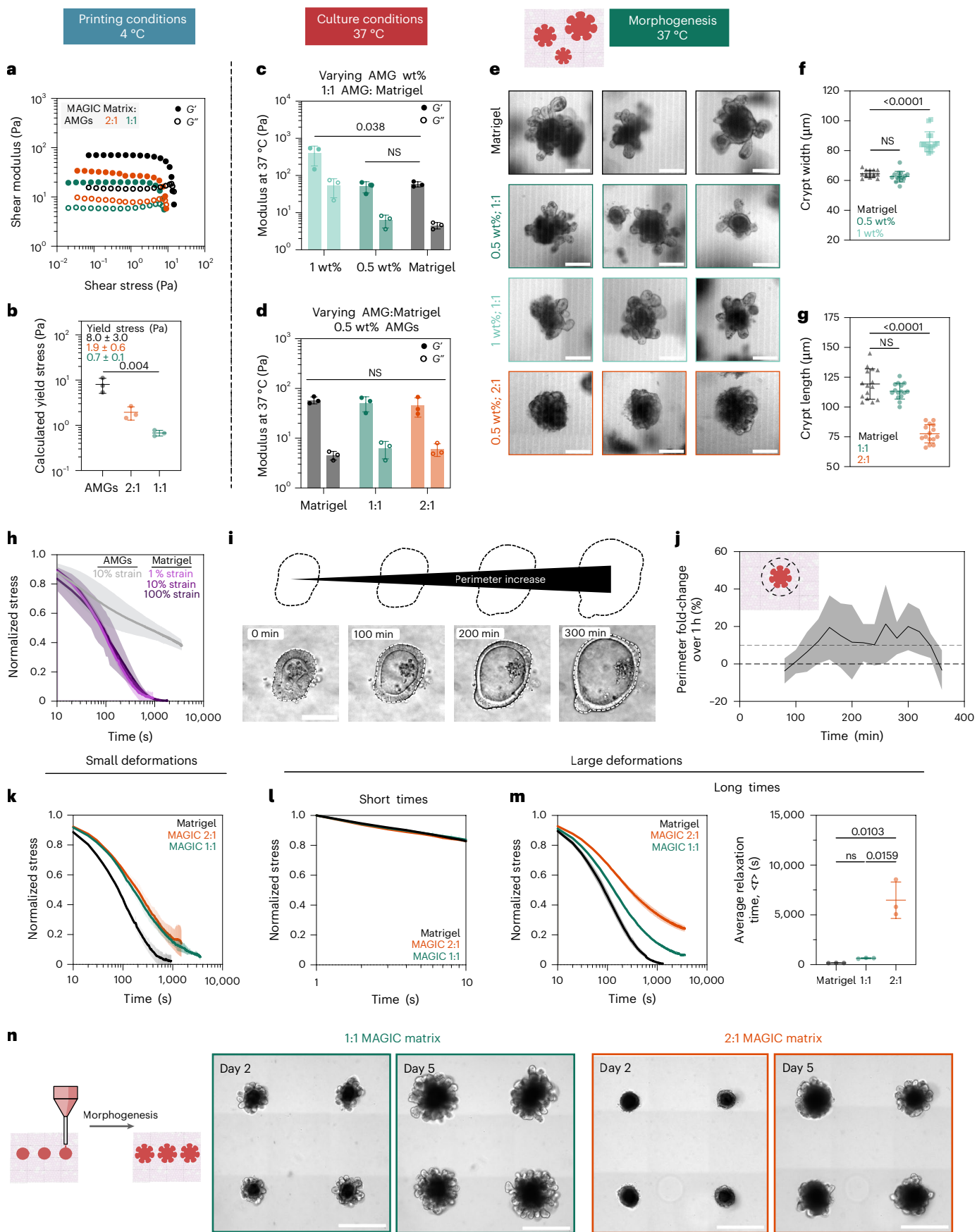
## A piezoelectric printhead enables precise, automated direct ‘writing’ of dense cell slurry bioinks

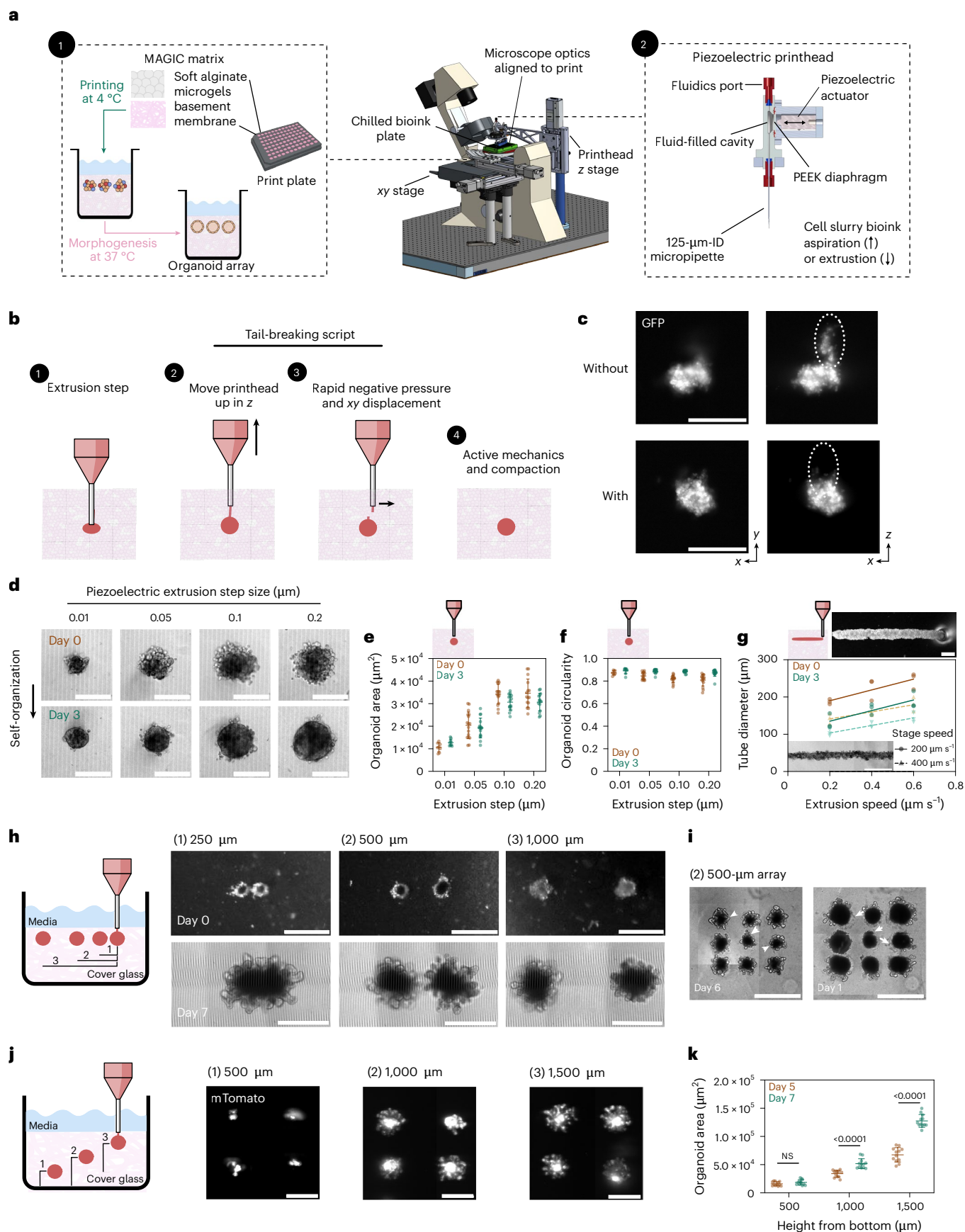
Organoid morphogenesis can be highly uniform when carefully controlling for initial conditions—for example, by starting from cell aggregates of similar initial size, geometry and composition<sup>17,27,42,43</sup>. We therefore

### Fig. 2 | Rheological properties of MAGIC matrices including low stiffness and stress relaxation drive gold-standard morphogenesis.

**a**, At 4 °C, oscillatory amplitude sweeps at 1 Hz reveal that various MAGIC matrix compositions behave as yield-stress materials, indicated by  $G'$  and  $G''$  cross-over. **b**, MAGIC matrices behave as Herschel–Bulkley fluids at 4 °C with yield-stresses calculated using a power-law model. **c**, Storage and loss moduli at 1 Hz and 1% strain of MAGIC matrices at 37 °C prepared from 1 wt% or 0.5 wt% AMGs. **d**, Storage and loss moduli at 1 Hz and 1% strain of MAGIC matrices at 37 °C prepared using different volume ratios of 0.5 wt% AMGs:Matrigel. **e**, Mouse intestinal organoids grown in pure Matrigel (top row) and MAGIC matrices of several compositions (lower rows) 5 days after seeding. Scale bars, 200  $\mu$ m. **f**, Quantification of organoid crypt width as a function of matrix composition. **g**, Quantification of crypt length as a function of matrix composition. **h**, Normalized stress-relaxation curves for undiluted 0.5 wt% AMG slurry at 10% strain or Matrigel over 1 h at 1%, 10% or 100% strain. **i**, Bright-field images and segmented cartoons simulating organoid growth over time in Matrigel. Scale bar, 100  $\mu$ m. **j**, Measurement of material strain at the organoid–ECM interface over time quantified using segmented organoid

perimeters. The dashed line at 10% strain represents the strain value used for most stress-relaxation measurements. **k**, Normalized stress-relaxation curves for Matrigel or MAGIC matrices over 1 h at 1% strain. **l**, Normalized stress-relaxation curves for Matrigel or MAGIC matrices over 10 s at 10% strain. **m**, Normalized stress-relaxation curves for Matrigel or MAGIC matrices over 1 h at 10% strain (left) and quantification of average relaxation time for each matrix using a stretched exponential model (right). **n**, Organoid array bioprinting experiments demonstrating similar impacts on crypt morphogenesis when MAGIC matrix compositions are used as bioprinting support baths. Scale bars, 500  $\mu$ m. For all rheological experiments, data shown are mean  $\pm$  s.d. from  $n = 3$  independently prepared replicates. For crypt length and width measurements, data shown are mean  $\pm$  s.d. on the median  $n = 15$  crypts from  $\geq 10$  organoids per matrix condition. For ECM strain during organoid growth, data shown are mean  $\pm$  s.d. of  $n = 9$  organoids. Statistical significance was determined by one-way ANOVA with Tukey's multiple comparisons (**b,c,m**) or Dunnett's multiple comparison (**f,g**); values shown for  $P$  determined by one-way ANOVA (**b**) or by multiple comparisons (**c,m,f,g**)  $< 0.05$ ; NS, not significant.





focused on developing bioprinting modalities that use MAGIC matrices together with pelleted single-cell bioinks at tissue-like densities of  $\geq 10^8$  cells  $\text{ml}^{-1}$  (ref. 44). We designed a piezoelectric printhead with fast pressure ramps that could directly aspirate small volumes with

high precision and without excess loss due to tubing and fluidics (that is, 'dead volume') (Fig. 3a and Supplementary Information, section 1). We leveraged a rapid voltage switch to 'break' cell slurry displacement from the printhead by applying a small negative pressure and  $xz$  displacement

**Fig. 3 | MAGIC matrix bioprinting utilizes a piezoelectric printhead to precisely aspirate and extrude cell slurry bioinks and can be programmed to generate organoid arrays.** **a**, Schematic illustrating the MAGIC matrix bioprinting platform, including the benefits of MAGIC matrix (left) and the piezoelectric printhead (right). **b**, The piezoelectric printhead and precise xyz control tolerate rapid pressure ramps and print plate movement, enabling scripts such as tail-breaking to improve print fidelity of viscous cell slurry bioinks. **c**, Representative fluorescent images of bioprinted spheroids with and without a tail-breaking script enabled by piezoelectric bioprinting through rapid changes in applied voltage and printhead position. Scale bars, 200  $\mu\text{m}$ . **d**, Representative bright-field images of bioprinted Caco-2 tissues at day 0 and day 3 post-print as a function of extrusion step size controlled via applied voltage. Data are representative of at least  $n = 9$  individual tissues per extrusion step condition. Scale bars, 200  $\mu\text{m}$ . **e, f**, Organoid area (**e**) and circularity (**f**) measured using maximum intensity projections of confocal z-stack images of GFP-expressing Caco-2 cell slurries. At both day 0 and day 3, organoid area significantly depends on extrusion step size until beyond 1.0  $\mu\text{m}$  as determined by one-way ANOVA with Tukey's multiple comparisons. Data shown are mean  $\pm$  s.e.m. of  $n \geq 9$  individual tissues per extrusion condition. At day 3, organoid circularity does not depend significantly on extrusion step size as determined by one-way ANOVA. **g**, Quantification of bioprinted tube diameter at day 0 and day 3 post-

printing as a function of both stage translation speed and extrusion step speed. Fit demonstrates that initial and final tube diameter are approximately linear functions of extrusion step speed for a given stage translation speed. Above, representative bright-field image of organoid tube during print. Scale bar, 200  $\mu\text{m}$ . Inset: representative tube exhibiting signs of lumenization 3 days after printing. Scale bar, 500  $\mu\text{m}$ . Data shown are  $n = 3$  bioprinted tubes per condition. **h**, Bioprinted mouse intestinal organoid pairs printed with 250-, 500- or 1,000- $\mu\text{m}$  centre-to-centre organoid spacing. Tissues printed close together ( $\sim 75$   $\mu\text{m}$  edge-to-edge) fuse (1), whereas tissues printed far enough apart ( $> 300$   $\mu\text{m}$  edge-to-edge) do not fuse (2, 3). Scale bars, 500  $\mu\text{m}$ . **i**, Organoids printed in arrays with 500- $\mu\text{m}$  pitch lack crypts between day 6 and 11. Arrowheads indicate crypts that formed close to the neighbouring organoids that are gone by day 11. Scale bars, 500  $\mu\text{m}$ . **j**, Maximum-intensity projections of intestinal organoid arrays bioprinted at different depths within MAGIC matrix (500  $\mu\text{m}$ , 1,000  $\mu\text{m}$ , or 1,500  $\mu\text{m}$  from the coverglass). Scale bars, 500  $\mu\text{m}$ . **k**, Organoids printed deeper in the matrix (1) do not significantly grow between days 5 and 7 post-print compared with organoids printed closer to the media interface (2, 3). Data shown are mean  $\pm$  s.d. of  $n = 12$  organoids per condition; statistical significance was determined by non-parametric *t*-test between day 5 and day 7; values shown for  $p < 0.05$ ; NS, not significant. Print plate illustration in a created in BioRender; Graham, A. <https://biorender.com/64hyq2k> (2026).

(Fig. 3b,c). We then applied this aspiration, extrusion and tail-breaking programme to script an automated spheroid bioprinting array. We first demonstrated that a Caco-2 cell slurry bioink could be delivered through a 125- $\mu\text{m}$  inside diameter (ID) nozzle to create spheroids of customizable dimensions (Fig. 3d). Spheroid area was a linear function of extrusion step (Fig. 3e). After bioprinting and self-organization in MAGIC matrices, Caco-2 spheroids underwent efficient lumenization (Fig. 3d). Although the initial geometry of extruded cell volume sometimes deviated from spherical, the high active surface tensions of these living inks rapidly correct surface irregularities through self-organization (Fig. 3f).

Cell slurries could also be printed as cylinders whose diameter could be tuned using both extrusion rate and stage speed, providing multiple engineering controls (Fig. 3g). Tube diameter was an approximately linear function of extrusion rate for the two stage speeds tested. Bioprinted Caco-2 cylinders self-organized similarly to spheres while maintaining their high aspect ratio (Fig. 3g, inset). These results demonstrate that a printhead using a piezoelectric actuator affords high volume precision and flexible control over bioink behaviour.

We explored the generality of bioprinting into MAGIC matrices by preparing mouse small intestine organoid arrays (Supplementary Movie 2). An important contributor to tissue and organoid heterogeneity in traditional ECM dome cultures is the disparity in microenvironmental conditions such as media access or interorganoid spacing. We therefore systematically varied either interorganoid spacing or z depth within the MAGIC matrix support bath using organoids printed with an initial average diameter of 200  $\mu\text{m}$ . Organoid pairs printed

with 250- $\mu\text{m}$  centroid-to-centroid spacing came into contact as they grew and fused over time, leading to one large organoid (Fig. 3h). Organoids spaced 500 or 1,000  $\mu\text{m}$  apart remained distinct and appeared to undergo normal morphogenesis for at least 7 days of culture. To examine the effect of interorganoid spacing on morphogenesis we printed  $3 \times 3$  arrays with 500- $\mu\text{m}$  spacing. Notably, after 11 days in culture, crypts only appeared at the periphery of the organoid array, while the centre organoid lost crypts (Fig. 3i). We hypothesize that this could be caused either by nutrient depletion or autocrine gradients<sup>45</sup>. Printing depth also had a profound effect on organoid phenotype, with organoids printed closer to the ECM–media interface growing the largest and forming the most crypts (Fig. 3j). Organoids printed too far from the ECM–media interface did not significantly grow over the same time (Fig. 3k). Together, these results highlight the importance of initial conditions and local microenvironment on organoid morphogenesis.

### MAGIC matrix enables the self-organization of many organoid types following bioprinting

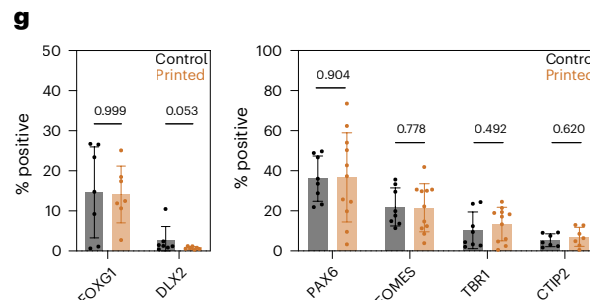
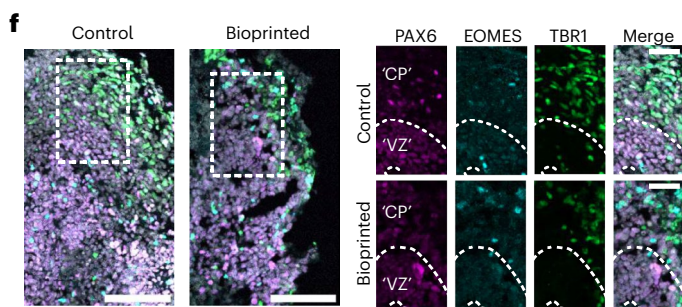
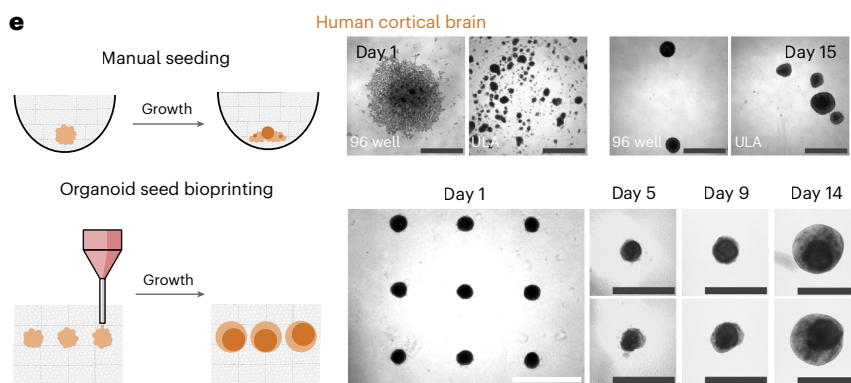
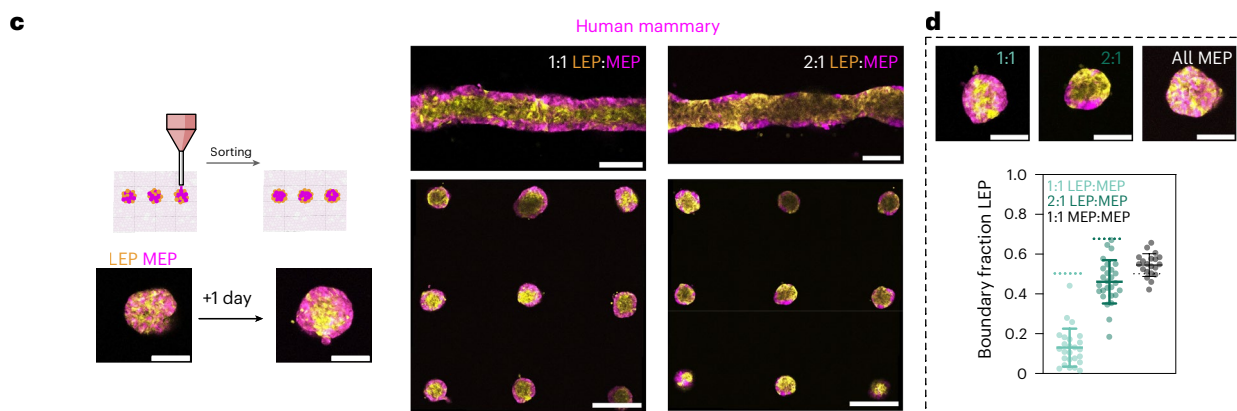
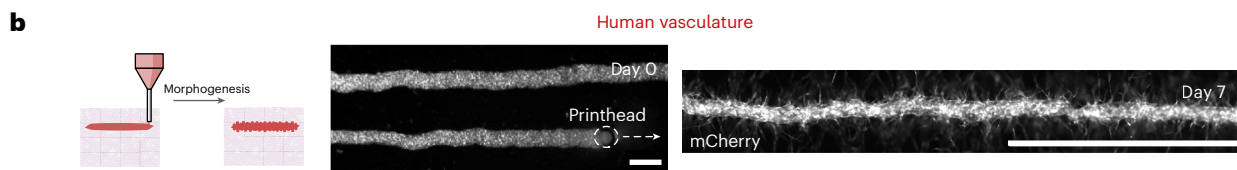
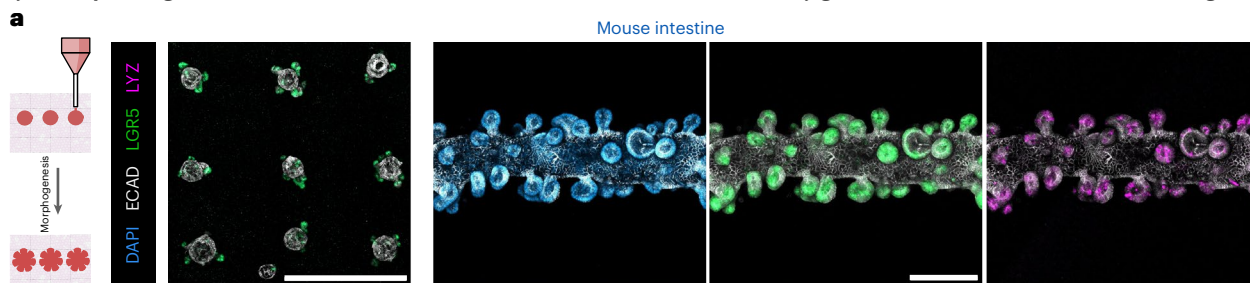
We next assessed whether organoid arrays exhibited expected self-organization when printed and cultured in MAGIC matrices, including mechanisms such as lumen formation, folding, budding, sprouting and sorting. For intestinal organoids, live imaging of a tdTomato reporter revealed crypt budding and protrusion within 2–3 days after printing in 96-well microplates (Extended Data Fig. 5). Organoids exhibited characteristic *Lgr5*<sup>+</sup> stem cell organization at the crypt base (Fig. 4a) and were positive for mature epithelial cell types, including Paneth cells (lysozyme) and enteroendocrine cells (chromogranin-A).

**Fig. 4 | MAGIC matrices promote self-organization of bioprinted tissues derived from the three primary germ layers.** **a**, Left: maximum-intensity projections of a representative *Lgr5*-GFP- and ECAD-stained intestinal organoid array 3 days after bioprinting. Scale bar, 1 mm. Right: maximum intensity projections 3 days after bioprinting intestinal organoid tubes stained with DAPI (left), *Lgr5*-GFP (middle) and LYZ (right). Scale bar, 200  $\mu\text{m}$ . **b**, Representative live images of bioprinted mCherry-expressing HUVEC tubes during printing (day 0) and following self-organization (day 7). Tubes over 2 mm long could be printed, with signs of vascular sprouting. Scale bars, 200  $\mu\text{m}$  (day 0) and 1 mm (day 7). **c**, Maximum-intensity projections of bioprinted spheroid arrays and tubes of HMEC organoids of different luminal and myoepithelial compositions. Organoids were allowed to sort for 1 day following printing. Scale bars, 500  $\mu\text{m}$  (arrays and tubes), 200  $\mu\text{m}$  (individual spheroids). **d**, Representative live images and quantification of luminal cell boundary occupation in bioprinted organoids as a function of composition. Dashed lines represent expected boundary

occupancy based on starting composition for mechanically equivalent cells<sup>43</sup>. Data shown are mean  $\pm$  s.d. for  $n \geq 20$  organoids analysed per composition. Scale bars, 200  $\mu\text{m}$ . **e**, Comparison of manually seeded and bioprinted induced pluripotent stem cell-derived human cortical brain organoids. Bright-field images of manually seeded cortical brain organoids in 96 or ultralow-attachment (ULA) well plates (top) or bioprinted arrays (bottom) over time. Scale bars, 1 mm (array), 200  $\mu\text{m}$  (manually seeded or individual bioprinted organoids). **f**, Left: 18- $\mu\text{m}$  maximum-intensity projections of control or bioprinted cortical organoid sections stained for cortical identity and neuronal differentiation. Scale bars, 100  $\mu\text{m}$ . Right: staining for cortical cell types. CP, cortical plate; VZ, ventricular zone. Scale bars, 50  $\mu\text{m}$ . **g**, Quantification of cortical identity (left) and neuronal differentiation (right) between bioprinted and manually seeded cortical brain organoids. Data shown are mean  $\pm$  s.e.m. of one quantified cryosection of  $n \geq 3$  organoids per marker from two separate differentiations; numbers shown are *p* values of multiple Mann–Whitney two-tailed tests.

Cell slurries derived from intestinal organoids also self-organized efficiently when printed in a cylindrical format<sup>17,42,46</sup>. Printed cords compacted, lumenized and folded radially, extending crypts within 2–3 days after printing.

Organoids of multiple developmental lineages that form through different programmes of self-organization behaved as expected following MAGIC matrix bioprinting. For example, mouse submandibular salivary gland, an ectodermal tissue that undergoes budding



morphogenesis<sup>47</sup>, exhibited characteristic multilobular structures within 3 days of printing and expressed ductal keratin 8 and basal keratin 14 (Extended Data Fig. 5). Human umbilical vein endothelial cell (HUVEC) vascular cords sprouted microvessels when printed into MAGIC matrix compositions supplemented with 1 mg ml<sup>-1</sup> collagen I<sup>46</sup> (Fig. 4b and Supplementary Movie 3). Vessels could be tuned in length and width up to and beyond the centimetre-scale (Supplementary Movie 4). We also evaluated the efficiency of cell sorting by printing spheroid arrays of patient-derived human mammary epithelial cells (HMEC) organoids, which comprise both the luminal cell (LEP) and myoepithelial cell (MEP) lineages<sup>43</sup> (Fig. 4c). Printed tissues robustly sorted across ~100- $\mu$ m distances to form bilamellar structures within 1 day, with the continuity of MEP coverage in the outer layer proportional to MEP composition in the organoid (Fig. 4d). HMECs printed as tubes also sorted robustly and maintained their initial tissue tubular geometry. Thus, MAGIC matrix bioprinting is compatible with a variety of self-organization mechanisms, including sorting, lumenization, migration and tissue folding.

The most common approach for defining the initial conditions of organoid culture is to aggregate dissociated tissue or stem cells using low-attachment plates<sup>1</sup>. However, it is unclear how aggregation dynamics impact downstream morphogenesis (Fig. 4e). We reasoned that MAGIC matrix bioprinting could enhance aggregate formation by forcing cells to interact in a common volume, and tested this by bioprinting human induced pluripotent stem cell (iPSC)-derived forebrain organoids<sup>48</sup>. We generated a bioink from 7-week differentiated organoids and printed into both MAGIC matrix or pure AMGs. Cortical brain organoids printed into MAGIC matrix exhibited the sprouting behaviour that is expected in rBM gels, and neuroepithelial bud formation, but lacked neuroectoderm (Extended Data Fig. 6)<sup>49</sup>. In contrast, cortical brain organoids printed in pure AMG slurry formed dense spheroids without protrusions and exhibited spatially organized neuroectoderm (Fig. 4e). These organoids were positive for the dorsal forebrain marker *FOXG1* and negative for the ventral forebrain marker *DLX2*, with ~15% dorsal identity and <1% ventral identity (Fig. 5f,g). Furthermore, the bioprinted cortical organoids demonstrated characteristic rosette self-organization with neural progenitors surrounding ventricular zone-like regions (PAX6+, ~35%), intermediate progenitor cells (EOMES+, ~20%) and deep layer excitatory neurons (TBR1+, ~10%; CTIP2+, ~5%) extending radially out from the apical surface (Fig. 5f). Overall, bioprinted organoids showed similar cell proportions to microwell-aggregated cortical organoids. Together, these results validate organoid bioprinting for efficient aggregate formation of iPSC-derived tissues.

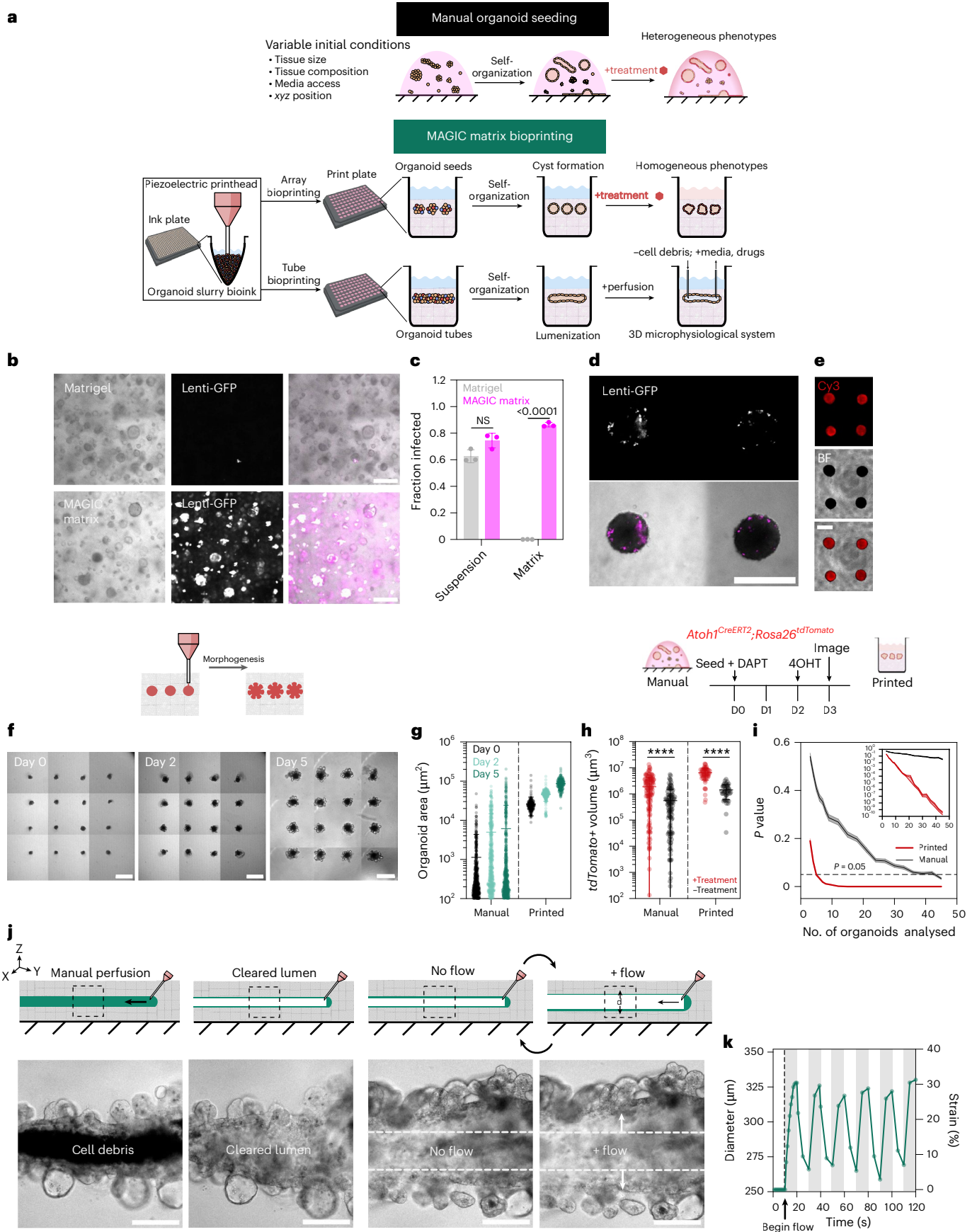
## Generation of high-throughput bioprinted organoid arrays for assay development

Similar to microwell methods, bioprinted organoid arrays hold great promise to increase the reproducibility and sensitivity of high-throughput assay development using CRISPR and drug screens<sup>16</sup>. However, bioprinted arrays have the added benefit of precise control over tissue geometry and other initial conditions (Fig. 5a). We compared organoid arrays prepared using MAGIC matrix bioprinting to traditional microwell aggregation. Bioprinted arrays had decreased variance in initial tissue size and improved circularity compared with microwells (Extended Data Fig. 7). To explore assays requiring genetic perturbations, we also transduced triple-negative breast cancer (TNBC) patient-derived organoids using H2B-GFP lentivirus (Fig. 5b). TNBC organoids showed no difference in infection efficiency when transduced in suspension and then plated in Matrigel or MAGIC matrix domes (Fig. 5c). However, when transducing TNBC organoids through the ECM by including lentivirus in the media after plating and gel cross-linking, infection efficiency was dramatically increased in MAGIC matrix, with nearly 90% GFP+ organoids compared to minimal-to-no infection in Matrigel. We hypothesize this is due to improved diffusivity or low protein binding afforded by low wt% (and therefore large pore size) AMGs in the composite support. Arrayed TNBC organoids were successfully transduced by including lentivirus in the media after bioprinting (Fig. 5d). TNBC organoid arrays were also highly amenable to transfection using Lipofectamine, showing strong RNA uptake as a function of both transfection time and amount of RNA delivered (Fig. 5e and Extended Data Fig. 7).

Achieving regularity among organoids with complex morphologies is a key challenge in developing organoid-based assays because it impacts the response of the organoids to genetic, mechanical and chemical perturbations<sup>16</sup>. We therefore quantified the timing and regularity of crypt morphogenesis after bioprinting in MAGIC matrix. Over the course of 5 days, bioprinted organoids synchronously self-organized, initially into lumenized cysts that further underwent budding morphogenesis (Fig. 5f). By contrast, manually seeded organoids showed far more heterogeneous morphologies over the same timeframe (Fig. 5g). Furthermore, bioprinted organoid arrays underwent more extensive and uniform morphogenesis, exhibiting a greater number of crypts with decreased variance compared with manually seeded organoids<sup>50</sup>. Organoids grown in manually seeded cultures using MAGIC matrix or pure Matrigel showed no difference in crypt number, indicating that more uniform initial conditions specifically contribute to improved maturity.

### Fig. 5 | MAGIC matrix bioprinting enables generation of high-throughput organoid arrays with improved statistical power and perfusable 3D microphysiological systems. a, Traditional manual methods of seeding organoids lead to heterogeneity in organoid growth and morphogenesis due to heterogeneity in starting tissue size, composition and microenvironment. By controlling for initial conditions such as cell number, media access and organoid spacing, bioprinting platforms facilitate rapid generation of reproducible organoid arrays or freeform 3D microphysiological systems. b, Live images of TNBC patient-derived organoids transduced overnight with GFP-expressing lentivirus while seeded in Matrigel (top) or MAGIC matrix (bottom). Scale bars, 200 $\mu$ m. c, Fraction of GFP+ organoids transduced in suspension before seeding or transduced after seeding for either ECM composition. Data shown are mean $\pm$ s.d. of $n = 3$ replicate ECM conditions; NS, not significant; \*\*\*\* $p < 0.001$ determined by two-tailed non-parametric $t$ -test between ECM conditions. d, e, Live images of bioprinted TNBC organoids transduced with GFP-expressing lentivirus overnight after printing (d) or transfected using Lipofectamine and Cy3-conjugated single-stranded non-coding small RNA for 24 h, 3 days after printing (e). Scale bars, 500 $\mu$ m. f, Live imaging of bioprinted intestinal organoid arrays following printing and after 2 and 5 days in culture. Scale bars, 500 $\mu$ m. g, Organoid area over time measured by segmentation for manual or bioprinted intestinal organoids; data shown are mean $\pm$ s.d. of $n \geq 190$ organoids

per time point. h, Top, experimental outline of phenotypic assay for inhibition of gamma-secretase. Red fluorescence indicates *Atoh1*+ secretory progenitors. Bottom, total red fluorescence volume per organoid in treated and untreated conditions from live images of bioprinted and manually seeded organoids treated with and without gamma-secretase inhibitor. For bioprinted arrays, data shown are mean  $\pm$  s.d. of  $n = 45$  organoids per condition. For manually seeded organoids, data shown are mean  $\pm$  s.d. of  $n \geq 135$  organoids per condition. \*\*\*\* $p < 0.0001$  determined by two-tailed non-parametric  $t$ -test. i, Bootstrapping analysis of statistical significance between treated and untreated conditions for either bioprinted or manually seeded organoids as a function of number of paired comparisons in a two-tailed non-parametric  $t$ -test. Curves shown are mean  $\pm$  s.e.m. for  $n = 512$  independent analyses. Inset: statistical significance approaches zero ( $<10^{-9}$ ) for bioprinted organoids using an equivalent number of comparisons because it takes manually seeded organoids to approach  $p = 0.05$ . j, Bright-field images of bioprinted intestinal organoid tubes that are manually perfused with a glass capillary attached to a micromanipulator and flushed to remove cell debris and access the lumen. Scale bars, 200  $\mu$ m. k, Quantification of tube diameter and resulting strain upon application and removal of fluid flow. Grey bars correspond to times when fluid flow was applied. Print plate illustrations in a created in BioRender; Graham, A. <https://biorender.com/64hyq2k> (2026).



## Bioprinted organoid arrays dramatically improve assay statistical power

The uniformity and reproducibility of MAGIC matrix bioprinting could dramatically improve the sensitivity of phenotypic assays. We tested this idea by treating intestinal organoids with a gamma-secretase inhibitor, *N*-[*N*-(3,5-difluorophenacetyl)-*L*-alanyl]-*S*-phenylglycine *t*-butyl ester (DAPT), which is known to increase the number of *Atoh1*+ secretory progenitors and decrease the number of stem cells<sup>51</sup>. Using an *Atoh1*<sup>CreERT2</sup>;*Rosa26*<sup>tdTomato</sup> reporter line, we treated bioprinted and manually seeded organoid cultures with DAPT for 2 or 3 days after seeding and imaged after 4 or 5 days (Extended Data Fig. 7). In manually seeded organoids, differences in overall tdTomato signal acquired by confocal microscopy were obscured by heterogeneity in organoid position, size and shape. In contrast, there was a clear change in morphology and increase in signal for DAPT-treated organoids in bioprinted arrays. We hypothesize this morphological change is linked to impacts of Notch inhibition on intestinal stem cell proliferation, which may be more obvious in bioprinted organoid arrays<sup>51</sup>.

Quantifying the volume of tdTomato-positive signal in each condition revealed that although there was a statistically significant increase in signal for both bioprinted and manually seeded organoids in treated versus untreated conditions, the effect size was substantially improved using bioprinted arrays (~3.7-fold increased difference between treated and untreated means) (Fig. 5h). Signal readout was also not normally distributed when manually seeded ( $p < 0.0001$  as determined by D'Agostino and Pearson test). Bioprinted organoids, in contrast, were more normally distributed and had decreased variance (printed coefficient of variance = 48% for treated and 58% for untreated; manual coefficient of variance = 127% for treated and 174% for untreated). Computing a post hoc power analysis ( $\alpha = 0.05$ ;  $\beta = 0.2$ ) with the given effect sizes and variances in each condition recommended  $n = 12$  printed organoids compared to  $n = 100$  manually seeded organoids. This nearly order-of-magnitude decrease in required comparisons emphasizes the attractiveness of MAGIC matrix bioprinting for rare tissues or subtle phenotypes.

To more precisely quantify how bioprinted arrays improved assay sensitivity, we performed bootstrapping on the bioprinted and manually seeded populations to calculate  $p$ -value as a function of the number of paired organoid comparisons (treated versus untreated). In the bioprinted arrays, we observed  $p$ -values below 0.05 after comparing only five organoids; in manually seeded organoid cultures, 45 comparisons were required to reach the same statistical significance (Fig. 5i).  $P$ -values for bioprinted organoids continued to decrease with additional comparisons approaching  $p \approx 10^{-10}$  after 45 comparisons—the same number of organoids necessary to reach a  $p$ -value of 0.05 in manually seeded organoids. This  $10^8$ -fold improvement highlights the potential of these bioprinted organoid arrays to detect subtle phenotypes in chemical, microenvironmental and genetic screens.

## Flexible production of 3D perfusable organoid tubes

Given the importance of fluid flow and both static and cyclic stress during processes such as peristalsis<sup>52</sup>, we examined whether mouse intestinal organoid tubes could be perfused following their lumenization and crypt morphogenesis (Fig. 5j). Using glass capillaries, we pierced the tissue lumen and introduced fluid using a syringe to clear internal cellular debris. By applying oscillatory fluid flow we could simulate cyclic expansion and contraction as might be experienced during peristalsis (Fig. 5k and Supplementary Movie 5). We observed radial expansion over ~30% of the perfused tubes at peak pressure enabled by the high deformability of MAGIC matrices, and unlike cultures using materials with non-physiological stiffness such as polydimethylsiloxane. Thus, MAGIC matrix tube bioprinting enables access to the organoid lumen and the introduction of biophysical cues such as fluid shear and both static and cyclic stretch, key features of microphysiological systems,

while maintaining a free basal surface that ultimately can be interfaced with other tissue types.

## Discussion

Promoting reproducible and complex organoid morphogenesis requires biomaterials that mimic the dynamic boundaries encountered by tissue *in vivo* while also supporting engineering controls necessary for setting the initial conditions of culture. Here we developed and characterized a simple granular biomaterial that achieves both goals. MAGIC matrices are relatively simple in design, using off-the-shelf and well-characterized constituents. They are highly tunable and revealed unique relationships between the loss tangent at low strains and short timescales, and stress relaxation at higher strains and longer timescales. This was true for a variety of MAGIC matrix compositions, presenting a suite of 3D granular biomaterials with which to investigate rheological determinants of tissue behaviour. Previous studies have demonstrated that rheological properties such as storage modulus, loss modulus and stress relaxation are collectively important for symmetry breaking and morphogenesis in intestinal organoids but could not indicate whether stress relaxation was independently important. We revealed the critical importance of stress relaxation at longer timescales and larger strains, consistent with the large tissue deformations required during intestinal crypt morphogenesis. Our work and others further suggest that rBMs behave more like viscoelastic liquids over the length scales and timescales of self-organization, and this capacity to dissipate stress may be a key driver of morphogenesis<sup>9,53</sup>. To take advantage of these materials in preparing more uniform and complex tissues *in vitro*, we developed a piezoelectric printhead that precisely aspirates and extrudes cell slurries at tissue-like densities directly into MAGIC matrices, thereby allowing tissues to autonomously self-organize while minimizing variability.

Most synthetic ECMs have been designed for a particular organoid or tissue type. MAGIC matrices successfully promote the self-organization of mouse and human tissues from all major germ layers, including endoderm (intestinal), ectoderm (brain, mammary, salivary gland) and mesoderm (vasculature, fibroblasts). Focusing on intestinal organoids, we found remarkably increased homogeneity in structure and phenotype by a number of metrics, including growth, morphogenesis and maturation rate. This homogeneity yielded organoid arrays that were 'assay-ready' in only 2–3 days, compared to previous studies that produced organoids of similar homogeneity but required 5 days or more in culture<sup>16,54</sup>. In addition to intestinal organoids, all tissue types could be bioprinted and cultured in high-throughput arrays or as tubes with little-to-no changes in printing parameters or matrix composition, for example, including collagen or excluding Matrigel. By a variety of functional metrics, these organoids were indistinguishable from those cultured in pure Matrigel, suggesting that the unique mechanisms contributing to tissue folding, tissue budding and cell sorting necessary for the self-organization of these other tissue types are also supported in MAGIC matrix<sup>6,43,55</sup>. MAGIC matrix bioprinting resulted in dramatic improvements in assay statistical power, decreasing the predicted number of tissues required to identify a phenotype by nearly an order of magnitude or more compared with manual culture. Therefore, this platform presents opportunities to work with precious tissue sources such as primary patient biopsies in applications such as clinical drug screens.

Finally, these technologies provide a route to more complex and *in vivo*-like 3D microphysiological systems, for example by perfusing bioprinted organoid tubes. The regularity and scalability of these models could be combined with established perfusion and coculture methods without the drawbacks of artificial interfaces and geometries. These findings lay the foundation for building even more complex and reproducible models of human and animal development, homeostasis and disease.

## Online content

Any methods, additional references, Nature Portfolio reporting summaries, source data, extended data, supplementary information, acknowledgements, peer review information; details of author contributions and competing interests; and statements of data and code availability are available at <https://doi.org/10.1038/s41563-026-02519-4>.

## References

- Hofer, M. & Lutolf, M. P. Engineering organoids. *Nat. Rev. Mater.* **6**, 402–420 (2021).
- Beck, L. E. et al. Systematically quantifying morphological features reveals constraints on organoid phenotypes. *Cell Syst.* **13**, 547–560.e3 (2022).
- Huycke, T. R. et al. Patterning and folding of intestinal villi by active mesenchymal dewetting. *Cell* <https://doi.org/10.1016/j.cell.2024.04.039> (2024).
- Trentesaux, C., Yamada, T., Klein, O. D. & Lim, W. A. Harnessing synthetic biology to engineer organoids and tissues. *Cell Stem Cell* **30**, 10–19 (2023).
- Gjorevski, N. et al. Designer matrices for intestinal stem cell and organoid culture. *Nature* **539**, 560–564 (2016).
- Gjorevski, N. et al. Tissue geometry drives deterministic organoid patterning. *Science* **375**, eaaw9021 (2022).
- Chaudhuri, O., Cooper-White, J., Janmey, P. A., Mooney, D. J. & Shenoy, V. B. Effects of extracellular matrix viscoelasticity on cellular behaviour. *Nature* **584**, 535–546 (2020).
- Kratovich, M. J. et al. Engineered materials for organoid systems. *Nat. Rev. Mater.* <https://doi.org/10.1038/s41578-019-0129-9> (2019).
- Chrisnandy, A., Blondel, D., Rezakhani, S., Broguiere, N. & Lutolf, M. P. Synthetic dynamic hydrogels promote degradation-independent in vitro organogenesis. *Nat. Mater.* <https://doi.org/10.1038/s41563-021-01136-7> (2021).
- Chrisnandy, A. & Lutolf, M. P. An extracellular matrix niche secreted by epithelial cells drives intestinal organoid formation. *Dev. Cell* <https://doi.org/10.1016/j.devcel.2025.06.026> (2025).
- Yavitt, F. M. et al. In situ modulation of intestinal organoid epithelial curvature through photoinduced viscoelasticity directs crypt morphogenesis. *Sci. Adv.* **9**, eadd5668 (2023).
- Cruz-Acuña, R. et al. Synthetic hydrogels for human intestinal organoid generation and colonic wound repair. *Nat. Cell Biol.* **19**, 1326–1335 (2017).
- Hushka, E. A. et al. Fully synthetic hydrogels promote robust crypt formation in intestinal organoids. *Adv. Mater.* **37**, e09672 (2025).
- Nikolaev, M. et al. Homeostatic mini-intestines through scaffold-guided organoid morphogenesis. *Nature* **585**, 574–578 (2020).
- Sockell, A. et al. A microwell platform for high-throughput longitudinal phenotyping and selective retrieval of organoids. *Cell Syst.* **14**, 764–776.e6 (2023).
- Brandenberg, N. et al. High-throughput automated organoid culture via stem-cell aggregation in microcavity arrays. *Nat. Biomed. Eng.* **4**, 863–874 (2020).
- Brassard, J. A., Nikolaev, M., Hübscher, T., Hofer, M. & Lutolf, M. P. Recapitulating macro-scale tissue self-organization through organoid bioprinting. *Nat. Mater.* **20**, 22–29 (2021).
- Hinton, T. J. et al. Three-dimensional printing of complex biological structures by freeform reversible embedding of suspended hydrogels. *Sci. Adv.* **1**, e1500758 (2015).
- Lawlor, K. T. et al. Cellular extrusion bioprinting improves kidney organoid reproducibility and conformation. *Nat. Mater.* **20**, 260–271 (2021).
- Urciuolo, A. et al. Hydrogel-in-hydrogel live bioprinting for guidance and control of organoids and organotypic cultures. *Nat. Commun.* **14**, 3128 (2023).
- Caprio, N. D., Hughes, A. J. & Burdick, J. A. Programmed shape transformations in cell-laden granular composites. *Sci. Adv.* **11**, eadq5011 (2025).
- Claxton, N. L., Luse, M. A., Isakson, B. E. & Highley, C. B. Engineering granular hydrogels without interparticle cross-linking to support multicellular organization. *ACS Biomater. Sci. Eng.* **10**, 7594–7605 (2024).
- Bhattacharjee, T. et al. Writing in the granular gel medium. *Sci. Adv.* **1**, e1500655 (2015).
- Morley, C. D. et al. Quantitative characterization of 3D bioprinted structural elements under cell generated forces. *Nat. Commun.* <https://doi.org/10.1038/s41467-019-10919-1> (2019).
- Morley, C. D., Tordoff, J., O'Bryan, C. S., Weiss, R. & Angelini, T. E. 3D aggregation of cells in packed microgel media. *Soft Matter* **16**, 6572–6581 (2020).
- Kajtez, J. et al. Embedded 3D printing in self-healing annealable composites for precise patterning of functionally mature human neural constructs. *Adv. Sci.* <https://doi.org/10.1002/advs.202201392> (2022).
- Reynolds, D. S. et al. Microporogen-structured collagen matrices for embedded bioprinting of tumor models for immuno-oncology. *Adv. Mater.* <https://doi.org/10.1002/adma.202210748> (2023).
- Brunel, L. G. et al. Embedded 3D bioprinting of collagen inks into microgel baths to control hydrogel microstructure and cell spreading. *Adv. Healthc. Mater.* <https://doi.org/10.1002/adhm.202303325> (2024).
- Elosegui-Artola, A. et al. Matrix viscoelasticity controls spatiotemporal tissue organization. *Nat. Mater.* **22**, 117–127 (2023).
- Muir, V. G. et al. Influence of microgel and interstitial matrix compositions on granular hydrogel composite properties. *Adv. Sci.* <https://doi.org/10.1002/advs.202206117> (2023).
- Pérez-González, C. et al. Mechanical compartmentalization of the intestinal organoid enables crypt folding and collective cell migration. *Nat. Cell Biol.* **23**, 745–757 (2021).
- Yang, Q. et al. Cell fate coordinates mechano-osmotic forces in intestinal crypt formation. *Nat. Cell Biol.* <https://doi.org/10.1038/s41556-021-00700-2> (2021).
- Tallapragada, N. P. et al. Inflation-collapse dynamics drive patterning and morphogenesis in intestinal organoids. *Cell Stem Cell* **28**, 1516–1532.e14 (2021).
- Chaudhuri, O. et al. Substrate stress relaxation regulates cell spreading. *Nat. Commun.* **6**, 6365 (2015).
- Nam, S., Stowers, R., Lou, J., Xia, Y. & Chaudhuri, O. Varying PEG density to control stress relaxation in alginate-PEG hydrogels for 3D cell culture studies. *Biomaterials* **200**, 15–24 (2019).
- Borelli, A. N. et al. Stress relaxation and composition of hydrazone-crosslinked hybrid biopolymer-synthetic hydrogels determine spreading and secretory properties of mscs. *Adv. Healthc. Mater.* **11**, e2200393 (2022).
- Fan, W. et al. Matrix viscoelasticity promotes liver cancer progression in the pre-cirrhotic liver. *Nature* **626**, 635–642 (2024).
- Indana, D., Agarwal, P., Bhutani, N. & Chaudhuri, O. Viscoelasticity and adhesion signaling in biomaterials control human pluripotent stem cell morphogenesis in 3D culture. *Adv. Mater.* **33**, e2101966 (2021).
- Roth, J. G. et al. Tunable hydrogel viscoelasticity modulates human neural maturation. *Sci. Adv.* **9**, eadh8313 (2023).
- Nerger, B. A. et al. 3D hydrogel encapsulation regulates nephrogenesis in kidney organoids. *Adv. Mater.* <https://doi.org/10.1002/adma.202308325> (2024).
- Reyes, E. A. et al. Epithelial TNF controls cell differentiation and CFTR activity to maintain intestinal mucin homeostasis. *J. Clin. Investig.* **133**, e163591 (2023).

42. Todhunter, M. E. et al. Programmed synthesis of three-dimensional tissues. *Nat. Methods* **12**, 975–981 (2015).
43. Srivastava, V. et al. Configurational entropy is an intrinsic driver of tissue structural heterogeneity. Preprint at *bioRxiv* <https://doi.org/10.1101/2023.07.01.546933> (2023).
44. Ho, D. L. L. et al. Large-scale production of wholly cellular bioinks via the optimization of human induced pluripotent stem cell aggregate culture in automated bioreactors. *Adv. Healthc. Mater.* <https://doi.org/10.1002/adhm.202201138> (2022).
45. Shin, W. et al. Spatiotemporal gradient and instability of Wnt induce heterogeneous growth and differentiation of human intestinal organoids. *iScience* **23**, 101372 (2020).
46. Cabral, K. A. et al. Programming the self-organization of endothelial cells into perfusable microvasculature. *Tissue Eng. A* **29**, 80–92 (2023).
47. Viragova, S. et al. Inverse agonists of retinoic acid receptor/retinoid X receptor signaling as lineage-specific antitumor agents against human adenoid cystic carcinoma. *J. Natl. Cancer Inst.* **115**, 838–852 (2023).
48. Shin, D. et al. Thalamocortical organoids enable in vitro modeling of 22q11.2 microdeletion associated with neuropsychiatric disorders. *Cell Stem Cell* **31**, 421–432.e8 (2024).
49. Lancaster, M. A. & Knoblich, J. A. Generation of cerebral organoids from human pluripotent stem cells. *Nat. Protoc.* **9**, 2329–2340 (2014).
50. Montes-Olivas, S. et al. In-silico and in-vitro morphometric analysis of intestinal organoids. *PLoS Comput. Biol.* **19**, e1011386 (2023).
51. McKinley, K. L. et al. Cellular aspect ratio and cell division mechanics underlie the patterning of cell progeny in diverse mammalian epithelia. *eLife* **7**, e36739 (2018).
52. Chevalier, N. R. Physical organogenesis of the gut. *Development* **149**, dev200765 (2022).
53. Nam, S., Lee, J., Brownfield, D. G. & Chaudhuri, O. Viscoplasticity enables mechanical remodeling of matrix by cells. *Biophys. J.* **111**, 2296–2308 (2016).
54. Serra, D. et al. Self-organization and symmetry breaking in intestinal organoid development. *Nature* **569**, 66–72 (2019).
55. Cazares, O., Haque, A. S. & Klein, O. D. Salivary gland: a budding genius. *Dev. Cell* **56**, 2271–2272 (2021).

**Publisher's note** Springer Nature remains neutral with regard to jurisdictional claims in published maps and institutional affiliations.

**Open Access** This article is licensed under a Creative Commons Attribution 4.0 International License, which permits use, sharing, adaptation, distribution and reproduction in any medium or format, as long as you give appropriate credit to the original author(s) and the source, provide a link to the Creative Commons licence, and indicate if changes were made. The images or other third party material in this article are included in the article's Creative Commons licence, unless indicated otherwise in a credit line to the material. If material is not included in the article's Creative Commons licence and your intended use is not permitted by statutory regulation or exceeds the permitted use, you will need to obtain permission directly from the copyright holder. To view a copy of this licence, visit <http://creativecommons.org/licenses/by/4.0/>.

© The Author(s) 2026

<sup>1</sup>Department of Pharmaceutical Chemistry, University of California San Francisco, San Francisco, CA, USA. <sup>2</sup>Chan Zuckerberg Biohub SF, San Francisco, CA, USA. <sup>3</sup>Department of Orofacial Sciences, University of California San Francisco, San Francisco, CA, USA. <sup>4</sup>Department of Bioengineering, University of California Berkeley, Berkeley, CA, USA. <sup>5</sup>Weill Institute for Neurosciences, University of California San Francisco, San Francisco, CA, USA. <sup>6</sup>Department of Medicine, University of California San Francisco, San Francisco, CA, USA. <sup>7</sup>Graduate Program in Bioengineering, University of California San Francisco and University of California Berkeley, San Francisco, CA, USA. <sup>8</sup>Department of Chemical and Biomolecular Engineering, University of California Berkeley, Berkeley, CA, USA. <sup>9</sup>Department of Bioengineering and Therapeutic Sciences, University of California San Francisco, San Francisco, CA, USA. <sup>10</sup>Department of Mechanical Engineering, Stanford University, Stanford, CA, USA. <sup>11</sup>Department of Bioengineering, Stanford University, Stanford, CA, USA. <sup>12</sup>Department of Pediatrics, Cedars-Sinai Guerin Children's, Los Angeles, CA, USA. <sup>13</sup>Center for Cellular Construction, University of California San Francisco, San Francisco, CA, USA. ✉ e-mail: [rafael.gomez@czbiohub.org](mailto:rafael.gomez@czbiohub.org); [zev.gartner@ucsf.edu](mailto:zev.gartner@ucsf.edu)

## Methods

### MAGIC matrix preparation

Sodium alginate (Sigma, 9005-38-3) was dissolved at 1 wt% (typically 1 g into 100 ml) into preheated 60 °C sterilized double-distilled water and stirred for 2–4 h until the solution was homogeneous. In a separate flask, calcium carbonate was mixed at 0.2 wt% (typically 200 mg into 100 ml). The dispersed calcium carbonate suspension was added to the alginate solution and cooled to room temperature while stirring for 1 h, leading to 0.5 wt% alginate and 0.1 wt% CaCO<sub>3</sub>. Pure acetic acid (Sigma, 64-19-7) was slowly added in dropwise, at a 1:500 ratio (typically 400 µl) under constant stirring at 1,000 r.p.m. The solution increased in viscosity, indicating release of Ca<sup>2+</sup> ions and alginate cross-linking. The solution was left stirring overnight at 1,000 r.p.m. to shear the mixture, leading to microgel formation. The next day, this mixture was blended for 60 s on the 'high' setting using a Hamilton Beach commercial blender (BioSpec 908). The microgel mixture was then strained through a 100-µm filter to remove large particles. The filtered microgels were centrifuged at 20,000g for 20 min at 4 °C and the supernatant aspirated, followed by resuspension in 1× volume of DMEM:F12 (UCSF Cell Culture Facility) medium supplemented with penicillin/streptomycin, Primocin (Invivogen) and 2 mM NaOH, and stored at 4 °C overnight or until the day before use. The day before use, the mixture was again centrifuged under the same conditions and the media replaced with 2× volume of DMEM:F12 supplemented with penicillin/streptomycin, Primocin, 4% v/v HEPES (1 M, UCSF Cell Culture Facility) and 4% v/v NaHCO<sub>3</sub> (37 g l<sup>-1</sup> in water, pH 9.5 with NaOH). This mixture was left overnight, centrifuged the next day and the supernatant aspirated. The resulting packed microgels were considered an undiluted microgel slurry and stored at 4 °C until use.

Just before seeding or printing, the undiluted slurry was mixed in various ratios (typically 1:1 pipetted volume ratio) with liquid basement membrane (typically Growth Factor-Reduced Matrigel, Corning 354230) at 4 °C. This leads to the desired dilution of microgels in basement membrane, or MAGIC matrix, for seeding or printing. The matrix was kept cold throughout seeding or printing, and then moved to a CO<sub>2</sub> incubator at 37 °C for 5–10 min after seeding or printing to allow for basement membrane cross-linking. Cell culture media specific to the bioprinted tissue type was then added.

### Rheological measurements and analysis

All rheological measurements were performed using a 25-mm cone-and-plate geometry on an Anton Parr rheometer. For shear oscillatory measurements, both frequency and amplitude sweeps were performed, with constant 1% strain and 1-Hz frequency, respectively. Temperature sweeps were performed at 1% strain and 1-Hz frequency, with 60 s for temperature equilibration before each measurement. For reversible shear experiments, 1% or 100% strain was applied at 1 Hz for 1 min each. To calculate the specific yield-stress of each composition, unidirectional shear measurements were performed at 1% strain and the data were fit to a Herschel–Bulkley power-law model. The y intercept was used to determine the yield-stress. For stress-relaxation experiments, the same geometry was used to apply 1%, 10% or 100% strain over 1 h after cross-linking by temperature ramp for 5 min and sealing the hydrogels with mineral oil to prevent evaporation. Nanoindentation experiments were performed using an Optics11 Life Chiaro Nanoindenter with a 50-µm tip and a 0.5 N m<sup>-1</sup> cantilever on indentation mode with 5-µm indentation for 60 s.

### Intestinal organoid isolation

Intestinal organoids were generated from the duodenum of Lgr5<sup>DTR</sup> mice using previously described protocols<sup>41</sup>. Briefly, the proximal portion of the small intestine was isolated, filleted open and rinsed 2× in PBS + penicillin/streptomycin on ice. The tissue was then incubated in harvest buffer (PBS + penicillin/streptomycin + 2 mM DTT + 10 µM Y27632 + 1 mM EDTA) with gentle rocking on ice for 15 min. After 15 min,

the tissue was shaken for 1 min, transferred to crypt dissociation buffer (PBS + penicillin/streptomycin + 2 mM DTT + 10 µM Y27632 + 5 mM EDTA), and incubated for 1 h with gentle rocking on ice. The tissue was then shaken for 1 min, filtered through a 70-µm filter, rinsed with 5 ml of ice-cold basal medium (Advanced DMEM/F12 High Glucose, *N*-acetyl-L-cysteine, penicillin/streptomycin, Glutamax, HEPES) and enumerated. Approximately 1,000 crypts were plated per well in preheated 24-well plates in 50-µl Matrigel domes (356231, Corning) in ENR medium (Basal Medium, B27 Supplement, N2 Supplement, hrEGF (50 ng ml<sup>-1</sup>), Noggin (100 ng ml<sup>-1</sup>) and R-spondin conditioned medium).

### Intestinal cell and organoid culture

In general, cells or organoids were cultured according to standard protocols specific to that cell type. Caco-2 cells were cultured in DMEM + 10% FBS with media changes every 3–4 days and passaged once per week. For mouse proximal small intestinal organoids (gut organoids), organoids were cultured according to published protocols<sup>41</sup>. Briefly, gut organoids were cultured in 3D Matrigel domes on 24-well plates with 1 ml of ENR medium (EGF, Noggin, R-Spondin) for 4–7 days before passaging, with media changes every 2–4 days, depending on desired growth rate. For passaging, gut organoids were collected by mechanical dissociation of the Matrigel domes using 1 ml of cold basal medium and centrifuging. All centrifugation steps were performed at 160g and 4 °C for 4 min unless stated otherwise. The supernatant was aspirated, and the pellet was fragmented by pipetting up and down in 1 ml of basal medium BM using a non-filtered 10- to 100-µl pipette tip attached to the end of a 1,000-µl pipette tip to gently increase shear. The crypt fragments were collected by again centrifuging and the supernatant was aspirated. These fragments were resuspended in Matrigel, generally at a 1:4 or 1:6 split ratio (for example, 100 or 150 µl of Matrigel per 25-µl dome), and plated onto the bottom of 24-well plates. The plate was then inverted to prevent organoid settling, and the Matrigel allowed to polymerize in a CO<sub>2</sub> incubator at 37 °C for 5–10 min before adding 1 ml of warm ENR to each well. Gut organoids that were to be used for bioprinting were instead cultured in 1 ml ENRCV (with added 3 µM CHIR99021 and 1 mM valproic acid) to promote stem cell expansion. Salivary gland organoids were cultured using a similar method and medium as described above, using ENR supplemented with Y27632 (10 µM), Fgf10 (100 ng ml<sup>-1</sup>) and Fgf2 (25 ng ml<sup>-1</sup>) during maintenance and before printing. These organoids were also collected, dissociated and bioprinted using the same method as for the small intestine organoids.

### MAGIC matrix bioprinting workflow

Mouse intestinal organoids were collected for bioprinting 2–3 days after passaging, when the culture consists mostly of large clear cysts without substantial internal dead cell debris, and were prepared for single-cell dissociation as described previously<sup>17</sup>. For most bioprinting experiments, either 10 or 20 Matrigel domes were collected, yielding roughly 1–2 million cells. As during passaging, gut organoids were collected by mechanical dissociation of the Matrigel domes. After centrifugation, the pellet was gently resuspended in dissociation medium consisting of TrypLE Express (Gibco) supplemented with 2,000 U ml<sup>-1</sup> DNase I (STEMCELL Technologies), 1 mM *N*-acetylcysteine (Sigma), and 10 µM Y27632 (R&D Systems); 1 ml of this mixture was used for every ~5 wells used for printing, so generally 2 or 4 ml. The resuspended cells were incubated for 10 min in a water bath at 37 °C, with gentle shaking to agitate the pellet every 5 min. This mixture was neutralized by adding 8 ml or 16 ml basal medium supplemented with 10% FBS and gently pipetting up and down. Using a serological pipette, the cells were extruded dropwise through a 40-µm strainer to ensure a roughly single-cell suspension and filter debris. This mixture was centrifuged and the supernatant aspirated. The pellet was resuspended in 1 ml of ENR supplemented with 2.5 µM thiazovivin (Stemgent) and 2 mM EDTA (Gibco) and centrifuged again. This pellet was resuspended in ~30 µl of

of ENR with thiazovivin and EDTA and transferred to the 384-well collection plate on the bioprinter. Caco-2 cell slurries and salivary gland organoid slurries were prepared using the same protocol.

As described above, undiluted AMG slurry was mixed in a 1:1 pipetted volume ratio with liquid reconstituted basement membrane matrix (typically growth factor-reduced Matrigel, Corning 354230) at 4 °C to create MAGIC matrix. Then, 100  $\mu\text{l}$  of MAGIC matrix was then deposited into each well of a chilled 96-well plate (printbed plate) using a positive-displacement pipette to minimize bubbles. The printhead was then equipped with a 75-, 125- or 200- $\mu\text{m}$  ID plastic denudation micropipette (CooperSurgical, EZ-Tip) to use as the print nozzle. For most experiments, a 125- $\mu\text{m}$  ID tip was used. The 384-well bioink plate was centrifuged at 100g for 1 min to pellet the cell slurry bioink at the bottom of the well. This slurry was loaded via direct aspiration (of  $\leq 0.66 \mu\text{l}$ ) into the printhead nozzle to reduce dead volume and minimize the cell slurry volume required for printing. The motorized stage and print dimensions were calibrated manually and print parameters set using a custom MATLAB script controlling both the microscope stage and the printhead. Most frequently,  $3 \times 3$  or  $4 \times 4$  arrays of  $\sim 200\text{-}\mu\text{m}$ -wide organoid spheroids were deposited with 750- or 1,000- $\mu\text{m}$  interorganoid spacing.

After printing, the printbed plate was carefully moved to a 37 °C CO<sub>2</sub> incubator and allowed to sit for 5–10 min to allow for basement membrane cross-linking. Then, 200  $\mu\text{l}$  of warm ENR media with 2.5  $\mu\text{M}$  thiazovivin was added to each well. Media was changed every 2–4 days for spheroids, and every 2 days for tubes.

### Piezoelectric extrusion bioprinter design and operation

The piezoelectric printhead was mounted at a fixed *xy* position on a cantilevered arm fastened to a Zaber LRQ075 stage for motorized *z* control. A Leica microscope DMI8 stage controller held the print plate and provided micrometre-scale control of the *xy* position and the resulting print shape. Microscope integration provided real-time imaging during the printing process, which allowed rapid identification and diagnosis of printing issues should they occur. The bioink plate holder was mounted to two Zaber LSQ150 stages for motorized access to each bioink stored in a 384-well sample plate. Bioinks were loaded by directly aspirating a user-specified volume from a well so that only the printed volume was loaded—this is especially beneficial for precious samples such as biopsies or cell populations with insufficient bioink volume for loading typical commercial bioprinting syringes. Aspiration and extrusion was driven by Physik Instrumente's PI-841.10 piezo, which was mounted against a fluid-filled cavity with a polyether ether ketone diaphragm at the interface. A solenoid valve toggled the fluidic connection of the printhead cavity to a fluid reservoir, allowing the printhead to be filled, cleaned or purged, and then sealed for single-ended printing operation. This equipment results in a volume displacement resolution of  $\sim 10 \text{ pl}$ , a maximum aspiration/extrusion volume of  $\sim 660 \text{ nl}$ , and a maximum theoretical aspiration/extrusion rate of  $\sim 300 \mu\text{l s}^{-1}$  (the actual rate and resolution will be highly dependent on the rheological properties of the bioink). The entire process, including imaging, motion control, piezopipetting and fluidics, was controlled using MATLAB. Custom printing protocols were scripted for maximum repeatability, efficiency and iterative troubleshooting (Supplementary Movie 2).

The printbed plate was chilled during the experiment using cold, dry compressed air to prevent MAGIC matrix cross-linking during printing without obscuring or wetting the optics. The printbed plate temperature was monitored using a thermocouple and kept at 4–8 °C. The bioink plate was cooled with a closed-loop recirculating chiller held at 5 °C. Before each printing experiment, a calibration procedure was completed. First, to passivate and increase the hydrophilicity of the inner tubing, cavity and pipette tip surfaces, the system was incubated for 10 min with a treatment solution consisting of phosphate-buffered saline (PBS), 10 mg  $\text{ml}^{-1}$  bovine serum albumin (BSA), 10 mg  $\text{ml}^{-1}$

Tetronic 90R4 (Sigma 435546 functional oligomer) and 5 mM EDTA to reduce adherence of cellular components and Matrigel. This procedure also reduced adherence of air bubbles, which increase the system's hydraulic compliance and compromise pipetting precision and responsivity. Next, the pipette tip was centred within the field of view using the manual centring screws on a Thorlabs CXY1 stage. The bioink plate wells were then centred relative to the pipette tip using a three-corner calibration scheme. Finally, with the desired ink well in place, the desired aspiration height of the printhead pipette tip was set, typically just above the bottom of the bioink well, to collect dense cell slurry.

Once the instrument was calibrated, a series of scripts executed the printing procedure according to user-specified parameters. These parameters were defined in an editable file of constants, and included specifications such as print shape and size, array formatting, and the rate and amount of bioink that was loaded. The first script prompted the user to define the print area by selecting four corners of a bounding box within the print well. The printed array or tubes were constrained by the bounding box so that the tip never collided with the well walls during printing. Next, the slurry was loaded from the ink well to the tip. The tip navigated to its calibrated loading height, then aspirated slurry according to the user-specified parameters. Next, the tip navigated to the bounding box and started printing the array or tubes. The array positions were computed according to user-specified row and column dimensions while staying within the bounding box. A small back-pressure was applied by changing the voltage applied to the piezo, immediately followed by a rapid *z*-axis offset, sometimes followed by an *xy*-axis offset, to detach the cell slurry from the tip after each bolus. In general, a negative extrusion step of 0.01  $\mu\text{m}$  and a *z*-axis translation of 100  $\mu\text{m}$  at 1 mm  $\text{s}^{-1}$  consistently detached the slurry with minimal disturbance to the printed bolus or tube. This process was repeated for each array element within a print well and could be programmed to repeat across multiple wells for any container geometry, including microplates, Petri dishes and chambered slides.

### Organoid size and crypt analysis

Quantification of organoid area and crypt number was performed based on binary masks constructed using Fiji/ImageJ. Masks were achieved by taking maximum *z* projections of all imaged organoids in the tdTomato+ channel, adjusting contrast, applying a Gaussian blur (5–20  $\mu\text{m}$ ) and adaptively thresholding. Following conversion to a mask, holes were filled and organoids were identified with Analyze Particles (excluding objects  $< 5,000 \mu\text{m}^2$ , parameter = exclude add). To quantify organoid area, the area metric was extracted with ROI Manager (measure). To further quantify the number of crypts, we used a MATLAB crypt counting software developed by Montes-Olivas et al.<sup>50</sup> Here, we had to filter out smaller, manually seeded organoids to maintain crypt-counting accuracy. Consequently, the organoids included in this analysis were biased toward larger organoids, of similar size to the bioprinted condition.

For microwell comparison experiments, Caco-2 cells were prepared as described above and counted using a haemocytometer to calculate the desired cells seeded per EZSphere (AG4860-900SP) microwell. Cells were centrifuged to pellet at the base of the microwells before Matrigel was added on top of the wells and allowed to solidify. Media was then added to the wells and seeded spheroids were imaged and analysed as described above. For area quantification, the median 80 detected objects per well were used from two wells per seeding condition to match the 80 microwells per well EZSphere density and to exclude imaging artefacts.

### Bioprinted tube perfusion

Bioprinted tubes were allowed to self-organize and form lumens for 3–7 days, with media changes every other day. Gut tubes were generally printed into #1.5 coverglass-bottomed chambered slides with one

chamber, to allow access with a glass capillary and micromanipulator. Aluminosilicate glass micropipettes with a long taper were prepared using a P-97 micropipette puller (Sutter Instruments). The pulled pipettes were cut 3–5 mm from the tip to get 10- to 25- $\mu\text{m}$ -diameter pipettes with jagged ends, and filled with PBS. Once patent lumens were visible, one end of a tube was cut with a razorblade to create an opening, and the other end was pierced with the capillary mounted on a Narishige MM-89 micromanipulator connected to a syringe. Applying pressure to the syringe induced liquid and debris flow toward the open end of the tube. Images were acquired using a 10 $\times$ /0.25 numerical aperture air objective on a Zeiss Axiovert 200M running SlideBook software. Tube diameter as a function of time was measured by manual thresholding of the tube and dividing the thresholded area by the imaged tube length to obtain an average tube diameter. This was performed over each frame of a video over multiple pulse cycles.

### Gamma-secretase inhibition experiment and analysis

*Atoh1*<sup>CreERT2</sup>;*Rosa26*<sup>tdTomato</sup> gut organoids were isolated from proximal mouse small intestine and cultured as described above. Organoids were bioprinted or manually seeded and immediately cultured in ENR supplemented with either 50  $\mu\text{M}$  DAPT (+treatment) or a DMSO vehicle control (–treatment). The media was changed on the second day, and 1  $\mu\text{M}$  4-hydroxytamoxifen (4-OHT, Sigma-Aldrich H7904) was added. On the third day after seeding, organoids were imaged using equivalent settings in high-throughput on a GE Healthcare IN Cell Analyzer 2200 confocal microscope in bright-field and 568-nm channels equipped with a 10 $\times$ /0.35 numerical aperture air objective. For microscopy images, a maximum intensity projection was created in the 568-nm channel to show the tdTomato+ signal, and a representative central focal plane was chosen in bright-field. For analysis, a custom Fiji macro was generated to identify and segment individual organoids. The tdTomato+ volume of each individual organoid was then calculated in Fiji using a custom thresholding macro. Bootstrapping and subsequent *p*-value quantification between treated and untreated conditions for either printing or manual seeding was performed using a custom R script<sup>43</sup> with 512 iterations at each number of pairwise organoids.

### Statistical analysis

Sample numbers for a given experiment are provided in each figure legend and were always  $n \geq 3$  independent replicates. Statistical analyses included non-parametric *t*-tests, one-way analyses of variance (ANOVAs) with Tukey's or Dunnett's multiple comparisons, normality tests, conventional power analysis using  $\alpha = 0.05$  and  $\beta = 0.2$ , and bootstrapping as described above. Statistical analysis was performed using GraphPad Prism 10 (*t*-tests, ANOVAs, normality, power analysis) or R (bootstrapping).

### Additional methods

Additional methods on the culture and characterization of intestinal, salivary gland, vascular, mammary, cortical and TNBC organoids are available in the Supplementary Information.

### Reporting summary

Further information on research design is available in the Nature Portfolio Reporting Summary linked to this article.

### Data availability

All source data is available at the online version of this article. Source data are provided with this paper.

### Code availability

Custom MATLAB scripts are available at Zenodo via <https://doi.org/10.5281/zenodo.18331666> (ref. 56).

## References

56. Khoo, M. W. L. & Gómez-Sjöberg, R. *czbiohub-sf/matlab-organoid-printer*: v1.0.1. *Zenodo* <https://doi.org/10.5281/zenodo.18331666> (2025).

## Acknowledgements

We thank S. Montes-Olivas for guidance in the use of her MATLAB crypt counting software. We thank K. Healy for providing rheological equipment. We thank M. Skylar-Scott and his group for providing technical input and assistance. This work was funded by the Chan Zuckerberg Investigator Program to Z.J.G., the UCSF Center for Cellular Construction (DBI-1548297), a CBCRP IDEA award, the NIDDK (R01DK126376), the NCI (R33CA297969), the NIDCR (RM1DE035338) and the NIBIB (K99EB037059). A.J.G. was supported by a Chan Zuckerberg Biohub Collaborative Postdoctoral Fellowship. V.S. was supported by the Zena Werb Memorial Fellowship through the Helen Diller Family Cancer Center at UCSF. Fluorescence-activated cell sorting was performed on a BD Aria 3, supported in part by HDFCCC Laboratory for Cell Analysis Shared Resource Facility through a grant from NIH (P30CA082103).

## Author contributions

A.J.G. and Z.J.G. conceptualized the embedded bioprinting material design and application. A.J.G., M.W.L.K., H.K., P.L., R.G.-S. and Z.J.G. conceptualized the bioprinter instrumentation. A.J.G. performed materials synthesis and characterization. M.W.L.K., P.L. and R.G.-S. designed and built the bioprinter hardware and wrote the software. A.J.G., V.S., S.V., K.M.H. and N.G. performed primary cell isolation, culture, microscopy, immunofluorescence and organoid experiments. A.J.G., M.W.L.K., H.K., G.H., N.T.B., L.P. and J.S.A. performed experiments to identify optimal bioprinting parameters. M.W.L.K. wrote custom scripts for bioprinting organoid arrays. A.J.G., V.S. and M.B. wrote custom scripts for microscopy and statistical analysis. K.P., C.D.M., S.K. and O.C. consulted on and provided experimental assistance with material characterization. V.S., S.V., K.M.H., N.G., J.M.R., N.C., T.J.N. and O.K. consulted on and provided experimental assistance with organoid isolation, characterization and application. A.J.G. and Z.J.G. wrote the manuscript, with review and feedback from all other authors.

## Competing interests

A.J.G., M.W.L.K., R.G.S., and Z.J.G. are coinventors on a patent regarding the design and application of the embedded bioprinting material and piezoelectric printhead (US provisional patent application 63/605,710). Z.J.G. is an equity holder in Provenance Bio. The remaining authors declare no competing interests.

## Additional information

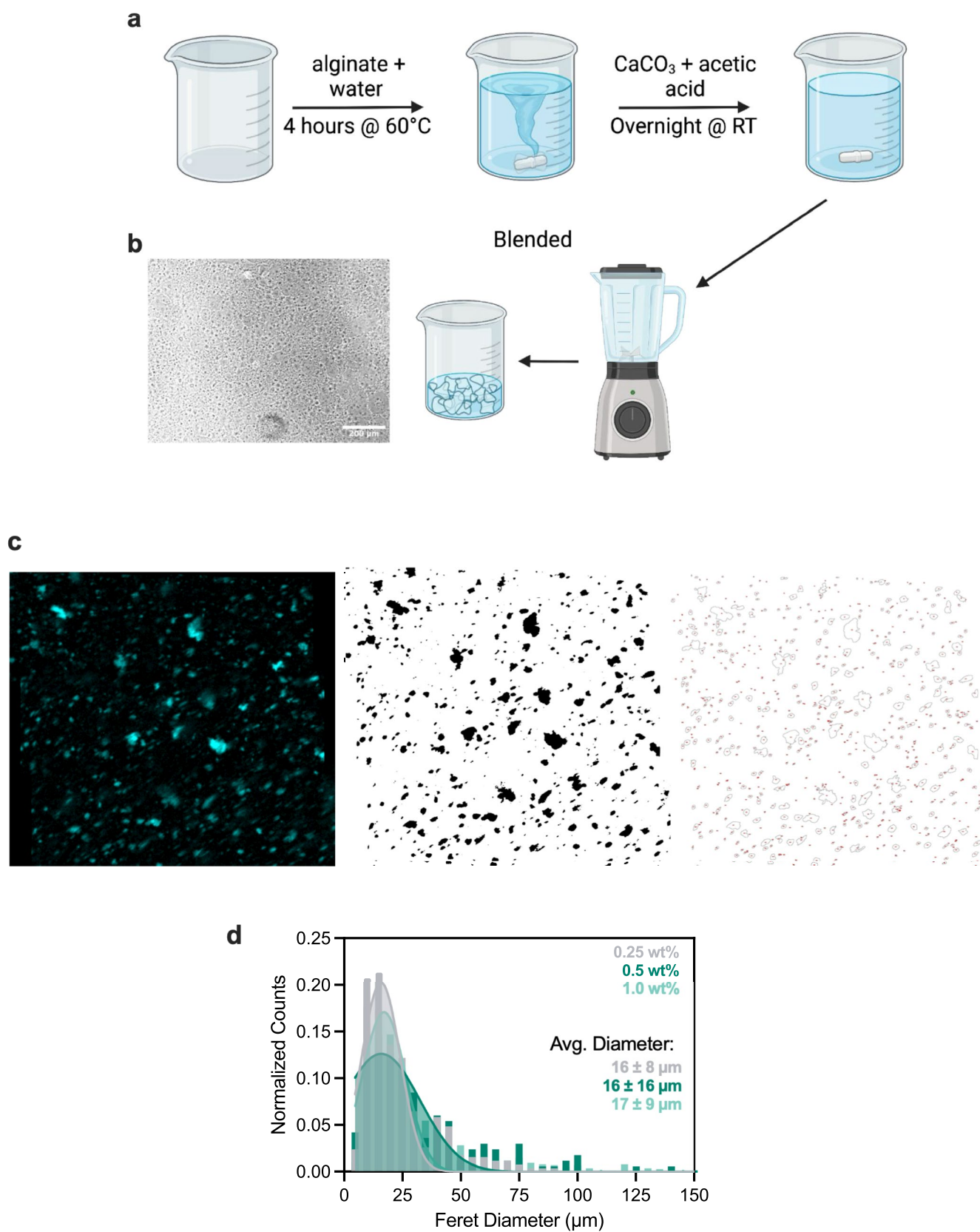
**Extended data** is available for this paper at <https://doi.org/10.1038/s41563-026-02519-4>.

**Supplementary information** The online version contains supplementary material available at <https://doi.org/10.1038/s41563-026-02519-4>.

**Correspondence and requests for materials** should be addressed to Rafael Gómez-Sjöberg or Zev J. Gartner.

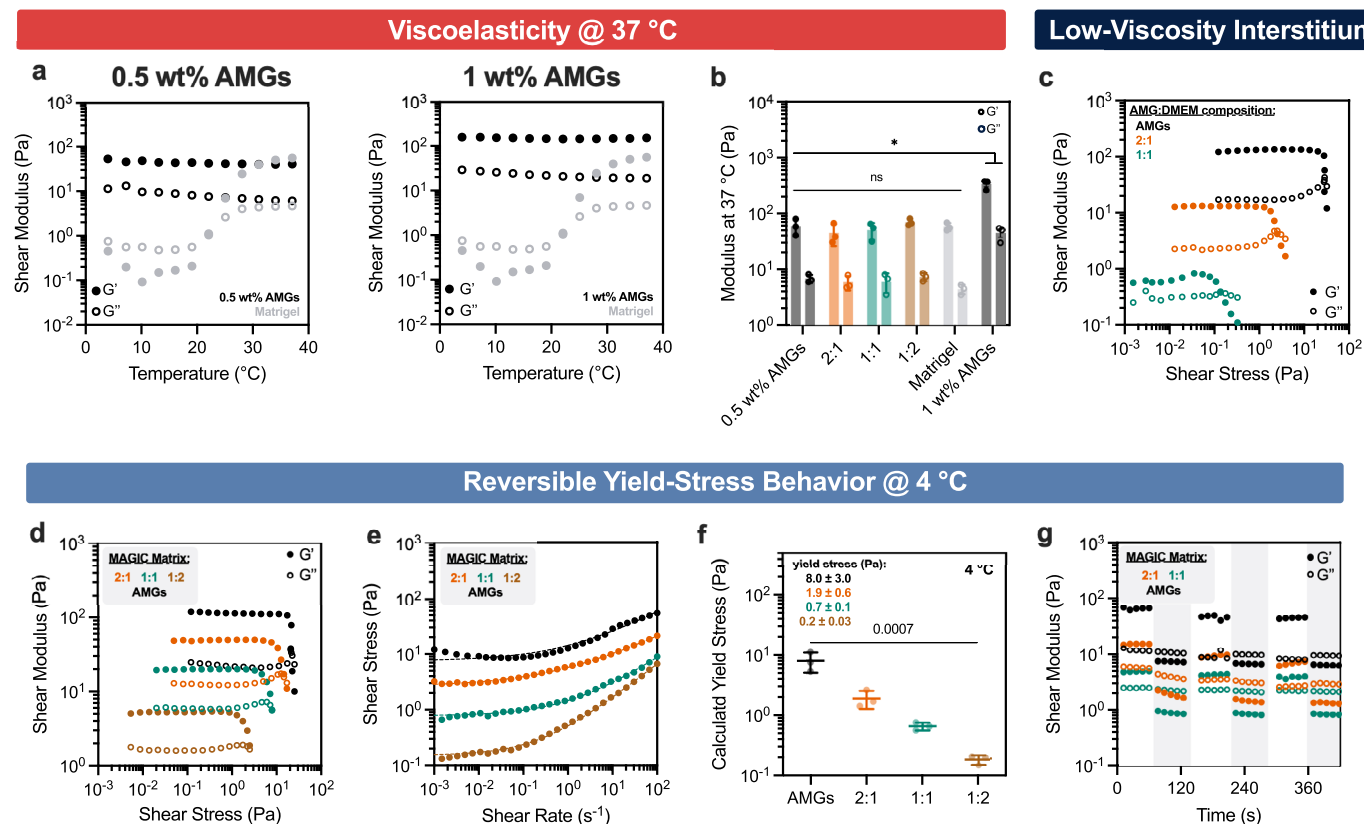
**Peer review information** *Nature Materials* thanks Thomas Angelini, Liliang Ouyang and the other, anonymous, reviewer(s) for their contribution to the peer review of this work.

**Reprints and permissions information** is available at [www.nature.com/reprints](http://www.nature.com/reprints).



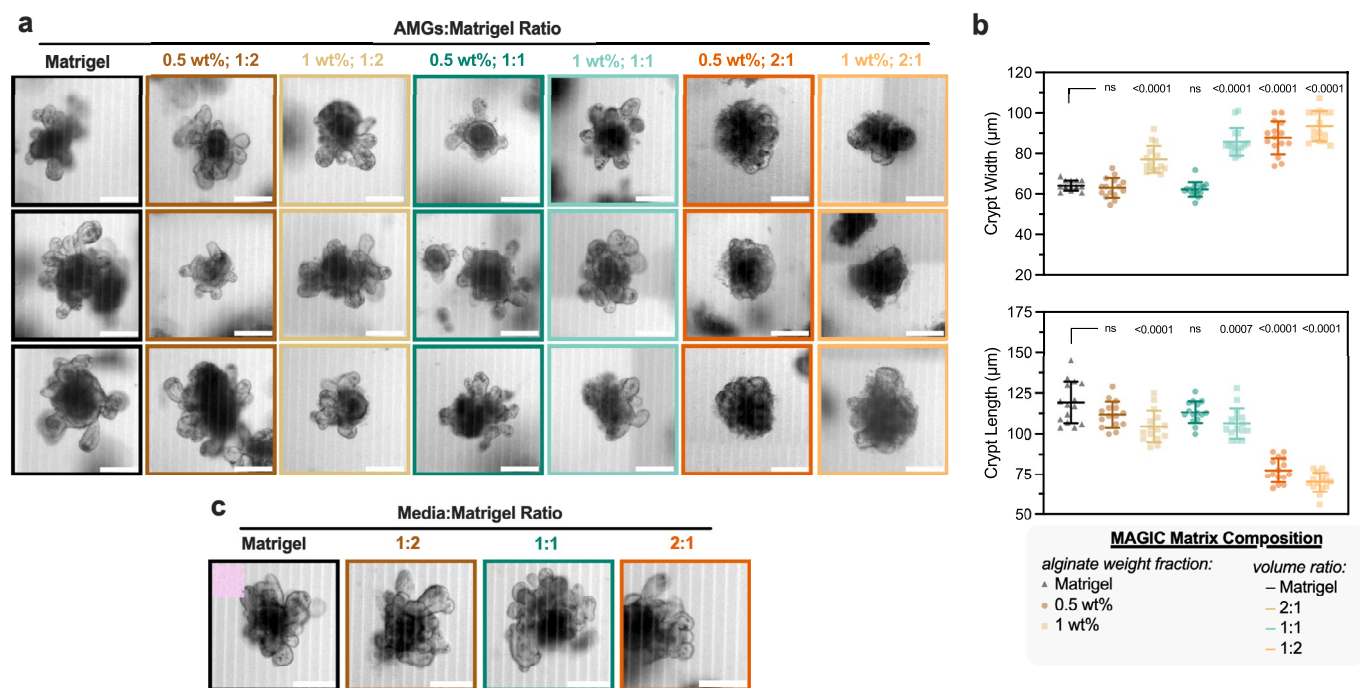
**Extended Data Fig. 1 | Alginate microgels are roughly cell-sized. a.** Cartoon workflow for preparation of alginate microgel slurry. **b.** Bright-field image of microgel slurry after synthesis, with nearly transparent microgels. Scale bar = 200 μm. **c.** Representative images outlining workflow for quantifying microgel size. The polyanionic alginate backbone was positively stained with DAPI and

segmented in Fiji to calculate particle diameter. **d.** Distribution of alginate microgel sizes fit to a Gaussian distribution. Data shown are mean ± SD from  $n = 3$  separate images from 3 separate fields of view for each alginate wt% and 3 independent AMG preparations.



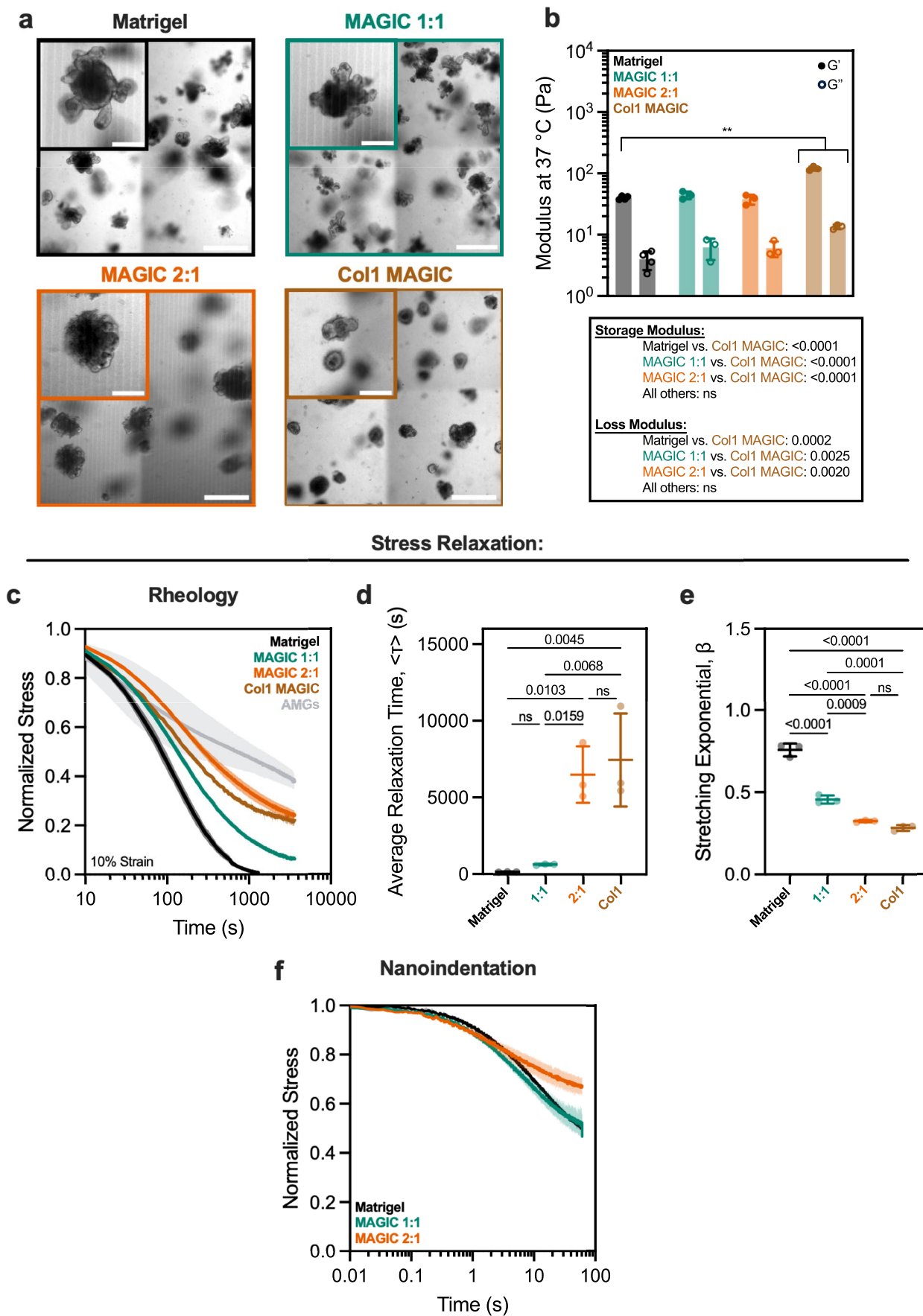
**Extended Data Fig. 2 | MAGIC matrices are tunable embedded printing and cell culture biomaterials.** **a.** Storage and loss modulus of (left) 0.5 wt% and (right) 1 wt% alginate microgel (AMG) pelleted slurry and Matrigel as a function of temperature. **b.** Storage and loss moduli of MAGIC matrix formulations at 37 °C using pelleted 0.5 wt% AMGs or (right) 1 wt% AMG slurry at 1 Hz and 1% strain. Data shown are mean  $\pm$  SD from  $n = 3$  independent microgel preparations. \* =  $p < 0.05$  for both storage and loss modulus of all MAGIC matrix formulations and 1 wt% AMG slurry compared to pure Matrigel as determined by one-way ANOVA with Dunnett's multiple comparisons. **c.** Oscillatory amplitude sweeps at 4 °C for various compositions of pelleted AMGs or AMGs diluted in cell culture media as a low-viscosity interstitium compared to Matrigel, which decreases jamming and yield-stress. 1:2 AMG:DMEM compositions did not exhibit yielding

behaviour. **d.** Oscillatory amplitude sweeps at 4 °C for various MAGIC matrix compositions show yielding behaviour indicated by  $G'$  and  $G''$  cross-over. Data shown are representative of  $n = 3$  independent microgel preparations. **e.** Unidirectional shear rate measurements at 4 °C fit to a Herschel–Bulkley power-law model. **f.** MAGIC matrix yield stress values calculated using Herschel–Bulkley fits in (D). Data shown are mean  $\pm$  SD of  $n = 3$  independent microgel preparations; statistical significance was determined by one-way ANOVA with P shown. **g.** Reversible yield-stress test wherein applied strain is alternated between 1% and 100% for a variety of MAGIC matrix formulations at 4 °C. Grey bars indicate areas of 100% strain. Cross-over and recovery of  $G'$  and  $G''$  indicates reversible viscoelastic behaviour. For **d**, **e**, and **g**, data are representative of  $n = 3$  independent microgel preparations.



**Extended Data Fig. 3 | MAGIC matrix composition impacts organoid morphogenesis.** **a.** Representative images of mouse intestinal organoids at 5 days after manually seeding into Matrigel and MAGIC matrices of varying AMG wt% and composition with Matrigel. MAGIC matrix compositions are represented as added volume ratio of AMGs:Matrigel. Scale bars = 200  $\mu\text{m}$ . **b.** Quantification of organoid crypt width (top) and crypt length (bottom) as a function of matrix

composition. Data shown are mean  $\pm$  SD on the median  $n = 15$  crypts from  $\geq 10$  organoids per matrix condition. Statistical significance was determined by one-way ANOVA with Dunnett's multiple comparison; values shown for  $p < 0.05$ ; ns = not significant. **c.** Representative images of organoids grown in Matrigel diluted at various volume ratios with mouse intestinal organoid growth medium. Scale bars = 200  $\mu\text{m}$ .

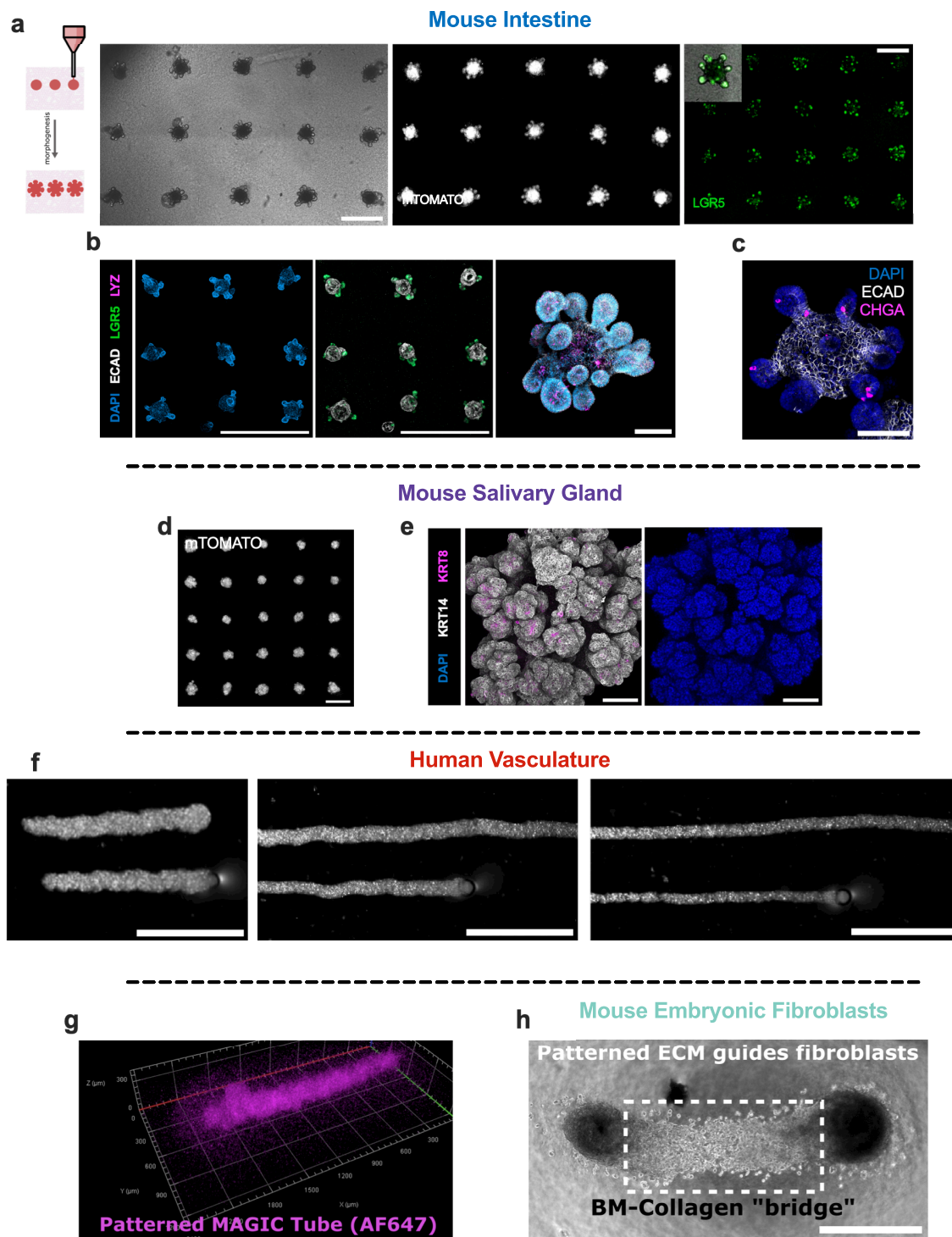


Extended Data Fig. 4 | See next page for caption.

**Extended Data Fig. 4 | ECM stiffness and stress relaxation determine phenotypes of crypt morphogenesis in intestinal organoids.**

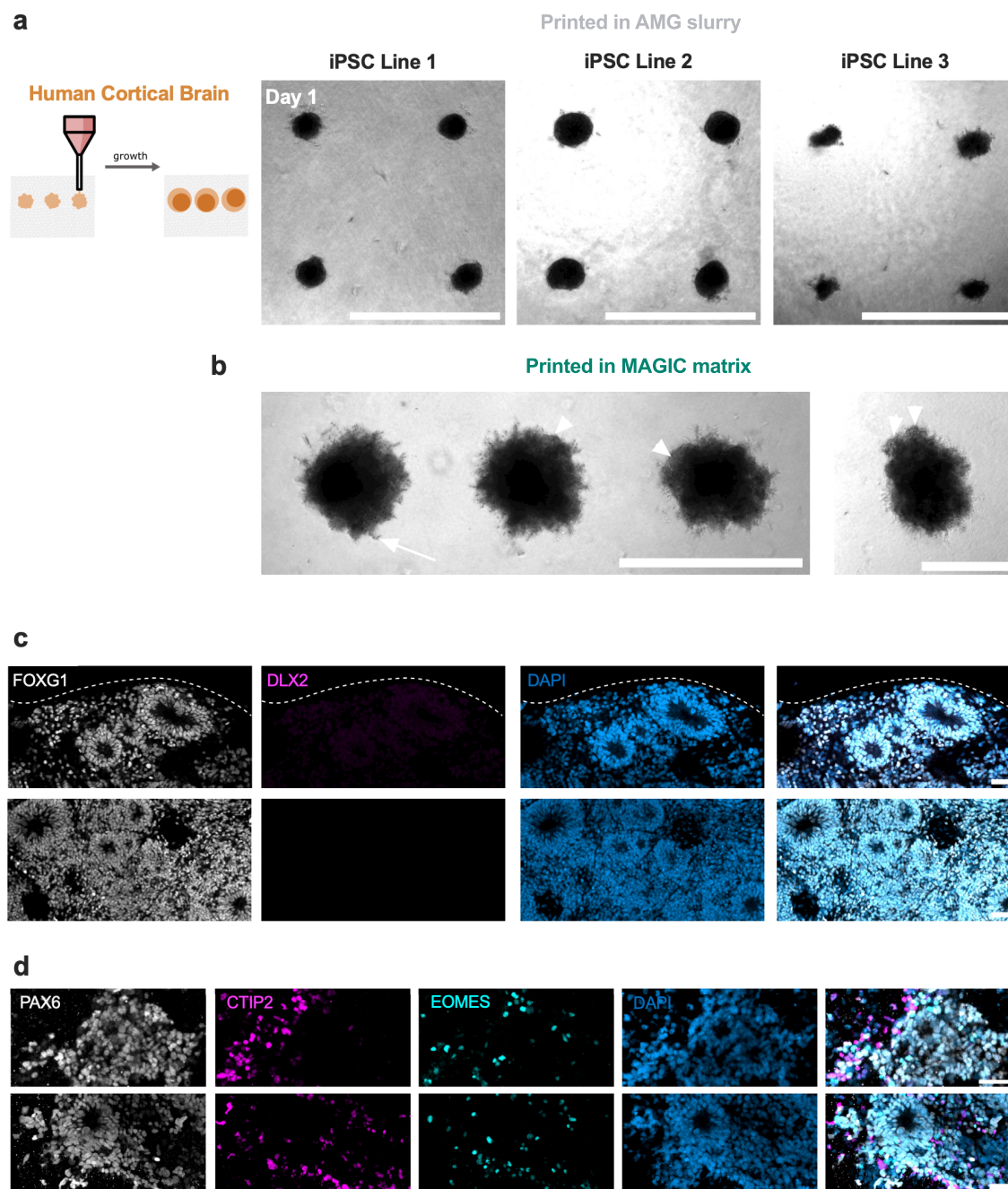
**a.** Representative images of mouse intestinal organoids at 5 days after manually seeding into Matrigel, MAGIC matrices, and collagen I-containing matrices. Collagen I-containing matrices were composed of 25% 4 mg/mL Bovine Col-1, 25% Matrigel, and 50% pure AMGs by added volume (final concentration of 1 mg/mL Col-1). Scale bars = 500  $\mu\text{m}$ . Insets show zoomed in view of representative organoids. Scale bars = 200  $\mu\text{m}$ . **b.** Storage and loss moduli of Matrigel, MAGIC matrix, and Collagen I-containing matrices at 37 °C, 1 Hz, and 1% strain. Table

summarizes statistical analysis. **c.** Normalized stress-relaxation curves for Matrigel, AMGs, MAGIC matrices, and Collagen I-containing matrices over 1 h at 10% strain. **d, e.** Quantification of average relaxation time (**d**) and stretching exponential (**e**) for each matrix determined using a stretched exponential model. **f.** Normalized stress-relaxation measurements of Matrigel and MAGIC matrices of various compositions using nanoindentation at 50  $\mu\text{m}$  indentation for 60 s. Data shown are mean  $\pm$  SD from  $n = 3$  independent ECM preparations. Statistical significance was determined by one-way ANOVA with Tukey's multiple comparisons with  $p$  values shown; \*\* =  $p \leq 0.01$ ; ns = not significant.



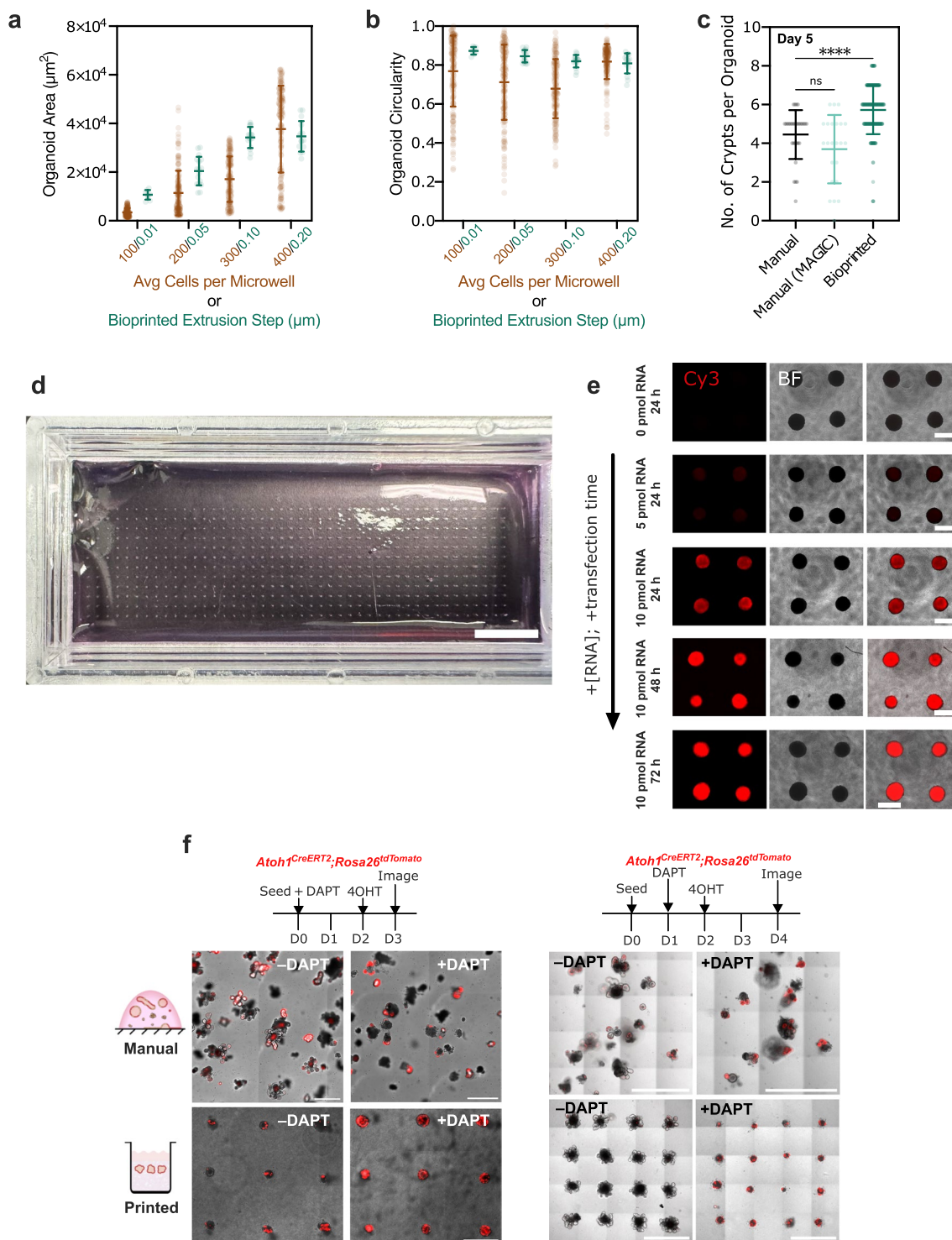
**Extended Data Fig. 5 | MAGIC matrices promote canonical self-organization of various organoid types from different developmental lineages. a.** Bright-field and fluorescent live images of mouse intestinal organoid arrays 2 days after bioprinting expressing either mTomato or *Lgr5*-eGFP. eGFP signal localizes to the base of the crypts, where *Lgr5*<sup>+</sup> stem cells should reside. Scale bars = 500  $\mu$ m. **b.** Left, maximum intensity projections of DAPI, *Lgr5*-GFP, ECAD-stained intestinal organoid arrays 3 days after bioprinting. Scale bar = 1 mm. Right, 3D rendering of fixed bioprinted intestinal organoids stained for DAPI, ECAD, and Paneth cells (LYZ). Scale bar = 200  $\mu$ m. **c.** Maximum intensity projection of DAPI, ECAD, and enteroendocrine cells (CHGA). Crypts protrude in all directions, highlighting fully 3D morphogenesis in MAGIC matrices. Scale bar = 200  $\mu$ m.

**d.** Live imaging of bioprinted salivary gland organoid arrays expressing mTomato. Scale bar = 1 mm. **e.** Immunofluorescence of fixed bioprinted salivary gland organoids showing presence of both basal (keratin 14) and ductal (keratin 8) cells. Scale bar = 100  $\mu$ m. **f.** Bright-field images of HUVEC cords bioprinted at different stage translation speeds highlighting control over vessel width. Scale bars = 1 mm. **g.** 3D rendering of an AF647-NHS stained MAGIC matrix tube printed into an AMG bath, highlighting the ability to pattern ECM. **h.** Bright-field images of mouse embryonic fibroblasts printed as two nodes with patterned Collagen 1 and MAGIC matrix printed between the nodes. Fibroblasts spread only into patterned area, highlighting spatial control over cell migration. Scale bar = 500  $\mu$ m.



**Extended Data Fig. 6 | Bioprinted hiPSC-derived cortical brain organoids exhibit matrix-dependent phenotypes and rosette organization.** **a.** Live images of human iPSC-derived cortical organoids from three different donors (methods) bioprinted into arrays using AMG support baths. Scale bar = 1 mm. **b.** Cortical organoids bioprinted in MAGIC matrices show sprouting (arrow)

and neuroepithelial budding (arrowheads). Scale bars = 1 mm (left) and 500  $\mu$ m (right). **c, d.** 20  $\mu$ m maximum intensity projections of bioprinted cortical organoids stained for **(c)** cortical identity and **(d)** neuronal differentiation. Scale bars = 50  $\mu$ m.



**Extended Data Fig. 7 | Bioprinted organoid arrays exhibit improved homogeneity and morphogenesis.** **a.** Organoid area and **b.** circularity measured using max intensity projections of confocal z-stack images of GFP-expressing Caco-2 cell slurries immediately after seeding in microwells or bioprinting. Data shown are mean  $\pm$  SEM of  $n \geq 9$  organoids per condition. **c.** Quantification of crypts per organoid for those manually seeded in Matrigel or MAGIC matrix, or bioprinted. Data shown are mean  $\pm$  SD of  $n \geq 30$  organoids; ns = not significant; \*\*\*\* =  $p < 0.0001$  determined by one-way ANOVA with

Dunnett's multiple comparisons. **d.** Picture of large ( $n = 528$ ) organoid array bioprinted into a chambered slide using MAGIC matrix. Scale bar = 10 mm. **e.** Live images of bioprinted TNBC organoid arrays transfected using Lipofectamine RNAiMAX and a Cy3-conjugated, single-stranded non-coding small RNA (36mer) at various concentrations and transfection times. Scale bar = 500  $\mu\text{m}$ . **f.** Live images of manually seeded and bioprinted *Atoh1*-tdTomato organoid arrays using two different DAPT treatment timelines. The left treatment timeline and images were used for bootstrapping and statistical analysis.

## Reporting Summary

Nature Portfolio wishes to improve the reproducibility of the work that we publish. This form provides structure for consistency and transparency in reporting. For further information on Nature Portfolio policies, see our [Editorial Policies](#) and the [Editorial Policy Checklist](#).

### Statistics

For all statistical analyses, confirm that the following items are present in the figure legend, table legend, main text, or Methods section.

n/a Confirmed

- The exact sample size ( $n$ ) for each experimental group/condition, given as a discrete number and unit of measurement
- A statement on whether measurements were taken from distinct samples or whether the same sample was measured repeatedly
- The statistical test(s) used AND whether they are one- or two-sided  
*Only common tests should be described solely by name; describe more complex techniques in the Methods section.*
- A description of all covariates tested
- A description of any assumptions or corrections, such as tests of normality and adjustment for multiple comparisons
- A full description of the statistical parameters including central tendency (e.g. means) or other basic estimates (e.g. regression coefficient) AND variation (e.g. standard deviation) or associated estimates of uncertainty (e.g. confidence intervals)
- For null hypothesis testing, the test statistic (e.g.  $F$ ,  $t$ ,  $r$ ) with confidence intervals, effect sizes, degrees of freedom and  $P$  value noted  
*Give  $P$  values as exact values whenever suitable.*
- For Bayesian analysis, information on the choice of priors and Markov chain Monte Carlo settings
- For hierarchical and complex designs, identification of the appropriate level for tests and full reporting of outcomes
- Estimates of effect sizes (e.g. Cohen's  $d$ , Pearson's  $r$ ), indicating how they were calculated

*Our web collection on [statistics for biologists](#) contains articles on many of the points above.*

### Software and code

Policy information about [availability of computer code](#)

Data collection

Data analysis

For manuscripts utilizing custom algorithms or software that are central to the research but not yet described in published literature, software must be made available to editors and reviewers. We strongly encourage code deposition in a community repository (e.g. GitHub). See the Nature Portfolio [guidelines for submitting code & software](#) for further information.

### Data

Policy information about [availability of data](#)

All manuscripts must include a [data availability statement](#). This statement should provide the following information, where applicable:

- Accession codes, unique identifiers, or web links for publicly available datasets
- A description of any restrictions on data availability
- For clinical datasets or third party data, please ensure that the statement adheres to our [policy](#)

## Research involving human participants, their data, or biological material

Policy information about studies with [human participants or human data](#). See also policy information about [sex, gender \(identity/presentation\), and sexual orientation](#) and [race, ethnicity and racism](#).

Reporting on sex and gender	n/a
Reporting on race, ethnicity, or other socially relevant groupings	n/a
Population characteristics	n/a
Recruitment	n/a
Ethics oversight	n/a

Note that full information on the approval of the study protocol must also be provided in the manuscript.

## Field-specific reporting

Please select the one below that is the best fit for your research. If you are not sure, read the appropriate sections before making your selection.

Life sciences       Behavioural & social sciences       Ecological, evolutionary & environmental sciences

For a reference copy of the document with all sections, see [nature.com/documents/nr-reporting-summary-flat.pdf](https://www.nature.com/documents/nr-reporting-summary-flat.pdf)

## Life sciences study design

All studies must disclose on these points even when the disclosure is negative.

Sample size	As a minimum, size was determined as $n \geq 3$ biological replicates or independent material formulations as is standard in the field.
Data exclusions	n/a
Replication	Replication was completed using biological replicates or independent material formulations performed on different days.
Randomization	n/a
Blinding	n/a

## Reporting for specific materials, systems and methods

We require information from authors about some types of materials, experimental systems and methods used in many studies. Here, indicate whether each material, system or method listed is relevant to your study. If you are not sure if a list item applies to your research, read the appropriate section before selecting a response.

### Materials & experimental systems

n/a	Involvement in the study
<input type="checkbox"/>	<input checked="" type="checkbox"/> Antibodies
<input type="checkbox"/>	<input checked="" type="checkbox"/> Eukaryotic cell lines
<input type="checkbox"/>	<input type="checkbox"/> Palaeontology and archaeology
<input type="checkbox"/>	<input checked="" type="checkbox"/> Animals and other organisms
<input type="checkbox"/>	<input type="checkbox"/> Clinical data
<input type="checkbox"/>	<input type="checkbox"/> Dual use research of concern
<input type="checkbox"/>	<input type="checkbox"/> Plants

### Methods

n/a	Involvement in the study
<input checked="" type="checkbox"/>	<input type="checkbox"/> ChIP-seq
<input checked="" type="checkbox"/>	<input type="checkbox"/> Flow cytometry
<input checked="" type="checkbox"/>	<input type="checkbox"/> MRI-based neuroimaging

## Antibodies

Antibodies used	Primary antibodies used include rat anti-ECCD2 (Thermo Fisher 131900), rabbit anti-LYZ (Thermo Fisher 129680), rabbit anti-CHGA (Novus Biologicals NB120-15160B), and chicken anti-GFP (Aves Labs GFP1010). Secondary antibodies were raised in goat and included Alexa Fluor 488 (Thermo Fisher A11039), Alex Fluor 568 (Thermo Fisher A11011), and Alexa Fluor 647 tags (Thermo Fisher A21247).
-----------------	---

Validation

Antibodies were validated for IF or IHC by each manufacturer.

## Eukaryotic cell lines

Policy information about [cell lines and Sex and Gender in Research](#)

Cell line source(s)

Caco-2 intestinal epithelium

Authentication

Cell lines were routinely karyotyped and checked for common contaminants such as mycoplasma.

Mycoplasma contamination

Cell lines routinely tested negative for mycoplasma.

Commonly misidentified lines  
(See [ICLAC](#) register)

n/a

## Palaeontology and Archaeology

Specimen provenance

*Provide provenance information for specimens and describe permits that were obtained for the work (including the name of the issuing authority, the date of issue, and any identifying information). Permits should encompass collection and, where applicable, export.*

Specimen deposition

*Indicate where the specimens have been deposited to permit free access by other researchers.*

Dating methods

*If new dates are provided, describe how they were obtained (e.g. collection, storage, sample pretreatment and measurement), where they were obtained (i.e. lab name), the calibration program and the protocol for quality assurance OR state that no new dates are provided.*

Tick this box to confirm that the raw and calibrated dates are available in the paper or in Supplementary Information.

Ethics oversight

*Identify the organization(s) that approved or provided guidance on the study protocol, OR state that no ethical approval or guidance was required and explain why not.*

Note that full information on the approval of the study protocol must also be provided in the manuscript.

## Animals and other research organisms

Policy information about [studies involving animals; ARRIVE guidelines](#) recommended for reporting animal research, and [Sex and Gender in Research](#)

Laboratory animals

Mouse organoids were collected from adult B6 mice.

Wild animals

*Provide details on animals observed in or captured in the field; report species and age where possible. Describe how animals were caught and transported and what happened to captive animals after the study (if killed, explain why and describe method; if released, say where and when) OR state that the study did not involve wild animals.*

Reporting on sex

*Indicate if findings apply to only one sex; describe whether sex was considered in study design, methods used for assigning sex. Provide data disaggregated for sex where this information has been collected in the source data as appropriate; provide overall numbers in this Reporting Summary. Please state if this information has not been collected. Report sex-based analyses where performed, justify reasons for lack of sex-based analysis.*

Field-collected samples

*For laboratory work with field-collected samples, describe all relevant parameters such as housing, maintenance, temperature, photoperiod and end-of-experiment protocol OR state that the study did not involve samples collected from the field.*

Ethics oversight

IRB and IACUC protocols were approved and followed.

Note that full information on the approval of the study protocol must also be provided in the manuscript.

## Clinical data

Policy information about [clinical studies](#)

All manuscripts should comply with the ICMJE [guidelines for publication of clinical research](#) and a completed [CONSORT checklist](#) must be included with all submissions.

Clinical trial registration

*Provide the trial registration number from ClinicalTrials.gov or an equivalent agency.*

Study protocol

*Note where the full trial protocol can be accessed OR if not available, explain why.*

Data collection

*Describe the settings and locales of data collection, noting the time periods of recruitment and data collection.*

## Dual use research of concern

Policy information about [dual use research of concern](#)

### Hazards

Could the accidental, deliberate or reckless misuse of agents or technologies generated in the work, or the application of information presented in the manuscript, pose a threat to:

- | No                                  | Yes                      |                            |
|-------------------------------------|--------------------------|----------------------------|
| <input checked="" type="checkbox"/> | <input type="checkbox"/> | Public health              |
| <input checked="" type="checkbox"/> | <input type="checkbox"/> | National security          |
| <input checked="" type="checkbox"/> | <input type="checkbox"/> | Crops and/or livestock     |
| <input checked="" type="checkbox"/> | <input type="checkbox"/> | Ecosystems                 |
| <input checked="" type="checkbox"/> | <input type="checkbox"/> | Any other significant area |

### Experiments of concern

Does the work involve any of these experiments of concern:

- | No                                  | Yes                      |   |
|-------------------------------------|--------------------------|---|
| <input checked="" type="checkbox"/> | <input type="checkbox"/> | Demonstrate how to render a vaccine ineffective                             |
| <input checked="" type="checkbox"/> | <input type="checkbox"/> | Confer resistance to therapeutically useful antibiotics or antiviral agents |
| <input checked="" type="checkbox"/> | <input type="checkbox"/> | Enhance the virulence of a pathogen or render a nonpathogen virulent        |
| <input checked="" type="checkbox"/> | <input type="checkbox"/> | Increase transmissibility of a pathogen                                     |
| <input checked="" type="checkbox"/> | <input type="checkbox"/> | Alter the host range of a pathogen  |
| <input checked="" type="checkbox"/> | <input type="checkbox"/> | Enable evasion of diagnostic/detection modalities                           |
| <input checked="" type="checkbox"/> | <input type="checkbox"/> | Enable the weaponization of a biological agent or toxin                     |
| <input checked="" type="checkbox"/> | <input type="checkbox"/> | Any other potentially harmful combination of experiments and agents         |

## Plants

### Seed stocks

Report on the source of all seed stocks or other plant material used. If applicable, state the seed stock centre and catalogue number. If plant specimens were collected from the field, describe the collection location, date and sampling procedures.

### Novel plant genotypes

Describe the methods by which all novel plant genotypes were produced. This includes those generated by transgenic approaches, gene editing, chemical/radiation-based mutagenesis and hybridization. For transgenic lines, describe the transformation method, the number of independent lines analyzed and the generation upon which experiments were performed. For gene-edited lines, describe the editor used, the endogenous sequence targeted for editing, the targeting guide RNA sequence (if applicable) and how the editor was applied.

### Authentication

Describe any authentication procedures for each seed stock used or novel genotype generated. Describe any experiments used to assess the effect of a mutation and, where applicable, how potential secondary effects (e.g. second site T-DNA insertions, mosaicism, off-target gene editing) were examined.